

# The ASCAT 6.25-km Wind Product

Jur Vogelzang, Ad Stoffelen, Richard D. Lindsley, *Member, IEEE*, Anton Verhoef, and Jeroen Verspeek

**Abstract**—The advanced scatterometer (ASCAT) wind data processor (AWDP) produces ocean surface vector winds from radar measurements by the ASCAT on board the Metop satellites. So far, the ASCAT-coastal product with a grid size of 12.5 km has been the one with the highest resolution. Version 2.4 of AWDP, released May 2016, offers the possibility to process wind data on a 6.25 km grid. In this paper, the true spatial resolution and accuracy of that product is assessed using various methods. The crucial parameter is the radius of the area used to aggregate individual backscatter observations to a wind vector cell (WVC) level. A value of 7.5 km, half of that for ASCAT-coastal, appears to be the best compromise between resolution and accuracy. Spatial responses from multiple radar cross-section measurements are combined to cumulative responses, and show that the ASCAT-6.25 product has a spatial resolution of about 17 km, better than the 28 km found for the ASCAT-coastal product. The accuracy of the ASCAT-6.25 product is estimated using comparison with collocated buoys, triple collocation analysis, and a new method based on spatial variances. These methods show consistently that the ASCAT-6.25 product contains about  $0.2 \text{ m}^2/\text{s}^2$  more noise in the wind components than the ASCAT-coastal product, due to the smaller number of individual measurements contributing to the average radar cross section in a WVC. The ASCAT-6.25 product is intended for applications that demand a spatial resolution as high as possible, like the study of dynamical mesoscale phenomena.

**Index Terms**—Radar, wind.

## I. INTRODUCTION

SCATTEROMETER-DERIVED winds form a reliable and accurate source of wind information at the surface of the oceans. They are assimilated on a routine basis in numerical weather prediction (NWP) models and are used operationally in nowcasting applications like monitoring of tropical cyclones, e.g., [1]. They are also used for driving ocean models, and to investigate climate variability in both the atmosphere and the ocean, e.g., [2]. Process studies into dynamical mesoscale phenomena like coastal jets and convective storms require as high a spatial resolution as possible.

The advanced scatterometer (ASCAT) is one of the instruments carried by the Metop series of polar orbiting satellites operated by the European Organisation for the Exploitation of Meteorological Satellites (EUMETSAT). ASCAT-A was launched

in 2006, ASCAT-B in 2012, and the launch of ASCAT-C is scheduled for 2018. ASCAT operates at C-band (frequency 5.3 GHz) and uses six fan-beam antennas, three at each side of the satellite. Two beams look forward at  $45^\circ$  azimuth with respect to the satellite moving direction, two look cross-track at  $90^\circ$  azimuth, and two look backward at  $135^\circ$  azimuth [3].

The ASCAT wind data processor (AWDP) is the standard software for deriving ocean surface wind vectors from the radar measurements [4]. AWDP is developed in the framework of the EUMETSAT NWP Satellite Application Facility (NWPSAF) and may be obtained free of charge upon registration from the NWPSAF web pages ([www.nwpsaf.eu](http://www.nwpsaf.eu)). AWDP is used by the Ocean and Sea Ice Satellite Application Facility to produce global near real-time wind products ([www.osi-saf.org](http://www.osi-saf.org)) on grid sizes of 25 and 12.5 km.

The basic output of the ASCAT instrument consists of individual measurements by each of the three beams of the radar cross section,  $\sigma_0$ , as generated by the on-board processor. The spatial extent of an individual  $\sigma_0$  value is determined by beam width in azimuth and by on-board processing in range. It is described by its spatial response function (SRF). ASCAT wind processing uses cross sections averaged to a wind vector cell (WVC) grid. This averaging (or aggregation) is done separately for the fore, mid, and aft beams. Its purpose is to reduce the noise inherent in radar measurements and to ensure that all beams cover the same area as much as possible. The spatial extent of an aggregated cross section is given by its cumulative spatial response function (CSRF).

The ASCAT-25 wind product has a WVC grid size of 25 km, but the aggregated radar cross section for each beam (fore, mid, and aft) is obtained by averaging all individual  $\sigma_0$  values that fall in a 100 km by 100 km square box centered at the WVC under consideration. The average is spatially weighted with a Hamming window, so most of the radar cross section comes from a 50 km by 50 km area. The aggregated radar cross sections in the Hamming-filtered ASCAT-12.5 product are calculated in a similar way, except that the grid size is 12.5 km and the size of the averaging area (or aggregation area) is 50 km [5].

A disadvantage in these products is that the WVCs must be located quite far from the coast in order to avoid land contamination in the aggregation area. For ASCAT-12.5, the coast line separation is about 35 km, which is too large for many coastal applications. The ASCAT-coastal product also has a grid size of 12.5 km, but the aggregated radar cross section is the unweighted average of all individual  $\sigma_0$  values that fall in a circular box with 15 km radius centered at the WVC. This is the same approach as followed earlier for the QuikScat scatterometer carried by the SeaWinds satellite [6]. The 15 km value of the aggregation radius was determined by spectral comparison in open sea with the ASCAT-12.5 product [5]. For the open ocean, the two products have the same quality and therefore ASCAT-12.5 was

Manuscript received June 30, 2016; revised September 23, 2016; accepted October 23, 2016. This work was supported by EUMETSAT as part of the Satellite Application Facility for Numerical Weather Prediction (NWP SAF). (Corresponding author: Jur Vogelzang.)

J. Vogelzang, A. Stoffelen, A. Verhoef, and J. Verspeek are with the Royal Netherlands Meteorological Institute (KNMI), De Bilt, The Netherlands, GA 3731 (e-mail: [Jur.Vogelzang@knmi.nl](mailto:Jur.Vogelzang@knmi.nl); [Ad.Stoffelen@knmi.nl](mailto:Ad.Stoffelen@knmi.nl); [Anton.Verhoef@knmi.nl](mailto:Anton.Verhoef@knmi.nl); [Jeroen.Verspeek@knmi.nl](mailto:Jeroen.Verspeek@knmi.nl)).

R. D. Lindsley was with the Microwave Earth Remote Sensing Laboratory, Brigham Young University, Provo, UT 84602 USA. He is now with the Remote Sensing Systems, Santa Rosa, CA 95401 USA (e-mail: [lindsley@remss.com](mailto:lindsley@remss.com)).

Color versions of one or more of the figures in this paper are available online at <http://ieeexplore.ieee.org>.

Digital Object Identifier 10.1109/JSTARS.2016.2623862

discontinued in April 2015. The smallest coastal distance in the ASCAT-coastal product is 20 km. Retrieving winds closer to the coast is currently not possible without accounting for the elongated shape of the SRFs (see Section III of this paper). EUMETSAT plans to implement a land fraction for each individual full-resolution measurement, which is computed from a land mask and the SRF [7].

In 2013, EUMETSAT started dissemination of a full-resolution radar cross-section product which contains the individual  $\sigma_0$  values generated by the on-board processor. It also contains a 6.25 km grid. This opened the possibility to define an operational ASCAT wind product on a 6.25 km grid processed in the same manner as the coastal product. The crucial parameter is the aggregation radius  $R$ : it must be smaller than 15 km (otherwise the true spatial resolution would not improve relative to ASCAT-coastal), but it must be large enough to capture enough individual  $\sigma_0$  values to ensure good radar cross-section statistics.

The approach in this study is less sophisticated than that outlined in [8], [9] and applied in [10], [11]. In those studies,  $\sigma_0$  is considered as a continuous field which is sampled by the scatterometer SRF. Deconvolution of the scatterometer measurements for each beam yields an estimate of the  $\sigma_0$  fields. These can be resampled on a fine grid. This approach allows for very high spatial resolutions, but its computational load makes it less attractive for operational use.

The aim of this paper is to characterize the true spatial resolution and accuracy of the new ASCAT-6.25 wind product as a function of  $R$  and to select the optimal choice for  $R$ . The true spatial resolution is estimated using the ASCAT SRF using the approach in [7]. The CSRf for each beam is obtained by summing the SRFs of all individual  $\sigma_0$  values within the aggregation area of a WVC, and normalizing the maximum value of the result to one. Similarly, the all-beam CSRf is obtained by summing the CSRfs of each of the three beams and again normalizing its maximum value to 1. The  $-3$  dB contour of the all-beam CSRf is a good indicator of the true spatial resolution. For ASCAT-coastal, the  $-3$  dB contour follows the edge of the aggregation area (the circular area with 15 km radius) quite well, leading to a true spatial resolution of about 28 km. For ASCAT-6.25, the CSRf is more elliptical, notably for the mid beam, due to the elongated SRF shape. The true spatial resolution varies with  $R$  and may range as low as 14 km for  $R = 5.0$  km, but the overlap between the beams is worse than for ASCAT-coastal and degrades with decreasing  $R$ . When beams do not overlap, they essentially observe slightly different parts of the ocean surface. As a result, wind variability will introduce variations in the average backscatter in each of the three beams, variations that are not consistent with the geophysical model function. This leads to so-called geophysical noise in the wind retrieval [12].

The ASCAT-6.25 product is shown to be noisier than ASCAT-coastal by using three methods: buoy comparison, triple collocation, and a novel method based on spatial variance analysis. The errors increase with decreasing  $R$ . All analyses give consistent results and indicate that a 7.5 km aggregation radius is a good compromise, giving an accuracy only slightly worse

than that of ASCAT-coastal and a spatial resolution of 17 km, which is clearly better than the 28 km found for ASCAT-coastal. To complete the quality assessment, the statistical consistency of ASCAT-6.25 with 7.5 km aggregation radius is shown to be slightly worse than that of ASCAT-coastal. This could be improved by better tuning of the error variances in the two-dimensional variational ambiguity removal scheme (2DVAR), both for ASCAT-6.25 and ASCAT-coastal, but that is considered outside the scope of this study.

The paper is organized as follows. The data used and some processing details are given in Section II. Section III deals with the spatial resolution based on the CSRf. Section IV contains the accuracy analysis of the ASCAT-6.25 winds retrieved for various values of the aggregation radius. A novel method for calculating the noise and its autocorrelation in the ASCAT-6.25 product relative to ASCAT-coastal is presented here, with some technical details in the Appendix. The comparison of statistical consistency is described in Section V. The results are discussed in Section VI, where it is argued that an aggregation radius of 7.5 km is a good compromise between spatial resolution and accuracy. Additionally, some suggestions for future improvement are presented here. The paper ends with conclusions in Section VII.

## II. DATA

In this study, we use all ASCAT-A data from August 2013. The data were processed on a 6.25 km grid with aggregation radii of 5, 7.5, 10, and 15 km. For the latter value, the product is identical with an oversampled ASCAT-coastal product. The ASCAT-6.25 product contains 162 WVCs per swath; 81 on each side of the satellite track. The KNMI quality flag, based on the inversion residual (MLE), was defined for the 7.5 km aggregation radius in the same manner as for the ASCAT-coastal and ASCAT-25 products. The inversion scheme of AWDP returns up to four solutions named ambiguities as well as the *a priori* probability of each ambiguity. As in the other AWDP products, the 2DVAR ambiguity removal scheme is used to select the most probable solution from these ambiguities.

During processing, the scatterometer winds are collocated with forecast winds from the ECMWF model as input for 2DVAR. The model winds, hereafter referred to as background, are interpolated quadratically in time and bilinearly in space to the scatterometer winds. The background winds are used as initial guess for the ambiguity removal, for monitoring purposes, and as data source in triple collocation. It must be stressed here that the background fields are not in the highest resolution available, but on a grid size of about 70 km, in order to guarantee continuity in operational 2DVAR processing. This grid size is sufficient for the purposes of this study.

Buoy data were obtained from the ECMWF MARS archive using all buoys not previously blacklisted. These buoy data are given as 10 min averages issued every hour, so the criteria for collocation with scatterometer data are a maximum temporal separation of 30 min and a maximum spatial separation of about 4.4 km (ASCAT-6.25 grid size divided by  $\sqrt{2}$ ). In cases where

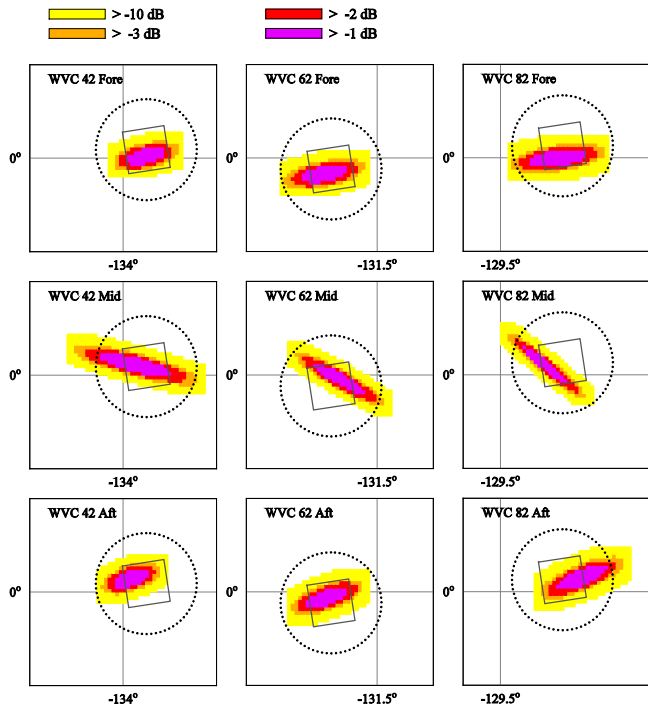


Fig. 1. Spatial response functions of a single ASCAT full-resolution radar cross-section measurement for the fore beam (top panels), mid beam (middle panels), and aft beam (bottom panels) for WVCs 42, 62, and 82 of the ASCAT-coastal product. The square box gives the WVC (size 12.5 km) and the dotted circle the boundary of the aggregation area (radius 15 km).

more collocations were found for the same buoy at the same time, the collocation closest in position was selected.

### III. SPATIAL RESOLUTION

The SRF for ASCAT, i.e., the spatial coverage of a single radar cross-section value in the full-resolution L1B EUMETSAT product, can be computed using the approach in [7]. As an illustration, Fig. 1 shows SRFs in dB of individual ASCAT radar cross sections, normalized to unit maximum value, with the colors indicating the value. SRFs are shown for the fore, mid, and aft beams (from top to bottom, respectively), and for WVC numbers 42, 62, and 82 (from left to right), corresponding respectively to lowest incidence angles, mid incidence angles, and highest incidence angles in the right-hand swath. The 12.5 km WVC is shown for reference, together with the boundary of the 15 km aggregation area. The WVCs lie on the right swath of an ascending orbit and are selected as close to the equator as possible in order to avoid distortion in the geographical grid.

Fig. 1 shows that the SRFs have an elliptical shape, caused by the antenna footprint, the range-gating, and the Doppler shift. The ellipses are quite elongated, notably for the mid beam. This is caused by on-board averaging of the antenna pulses: each full-resolution radar cross section is based on the running average of eight individual radar pulses. The chirps for the fore and aft beams go in different directions (low frequency to high frequency versus high to low), and Doppler shifts change the

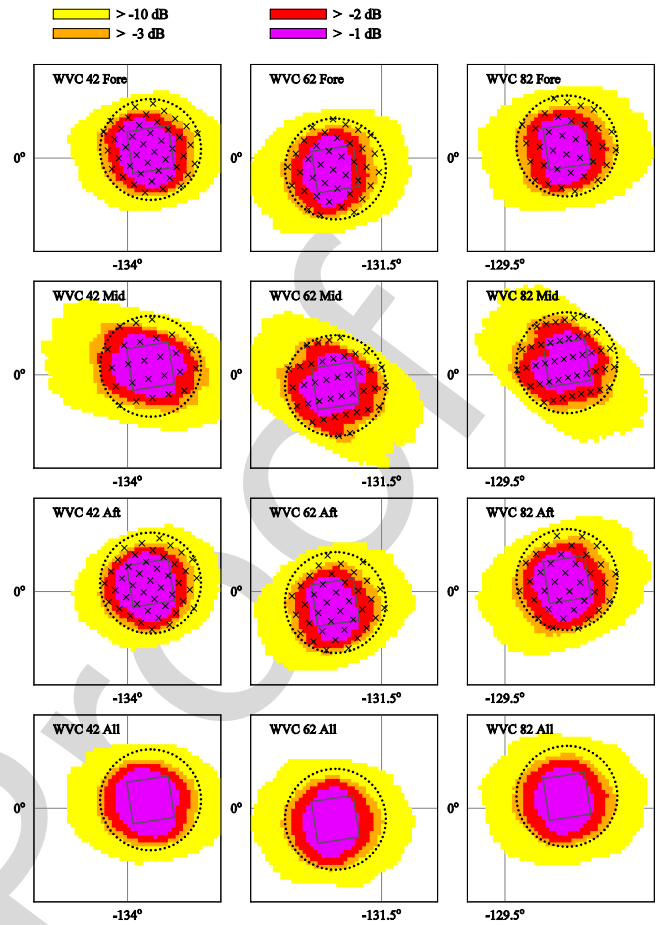


Fig. 2. Cumulative spatial response functions for ASCAT-coastal. The square box gives the WVC (size 12.5 km) and the dotted circle the boundary of the aggregation area (radius 15 km).

orientation of the ellipses in such a way that the fore and aft beam SRFs have almost the same orientation [7]. Fig. 1 also shows that the SRFs rapidly drop off to zero outside the  $-3$  dB contour.

For each beam separately, the CSRf for a WVC can be obtained by summing the SRFs contributing to that WVC and renormalizing to unit maximum value. The result for ASCAT-coastal is shown in Fig. 2. The colors indicate the CSRf value, the box represents the WVC boundary, the dotted circle the edge of the aggregation area, and the crosses the centers of the contributing SRFs. Note that the  $-3$  dB contour (CSRf equal to 0.501) follows the separation between orange and yellow, following quite well the edge of the circular aggregation area. The bottom row of panels in Fig. 2 shows the all-beam CSRf, i.e., the CSRf of all three beams combined, now without the centers of the contributing SRFs. The all-beam CSRf  $-3$  dB area also follows the edge of the aggregation area well, and its shape differs little from that of the CSRfs of the individual beams. This indicates good overlap between the three beams.

Fig. 3 shows the CSRf for ASCAT-6.25 with 7.5 km aggregation radius. As in Fig. 2, the WVC, the aggregation area boundary, and the contributing SRF centers are also shown, and

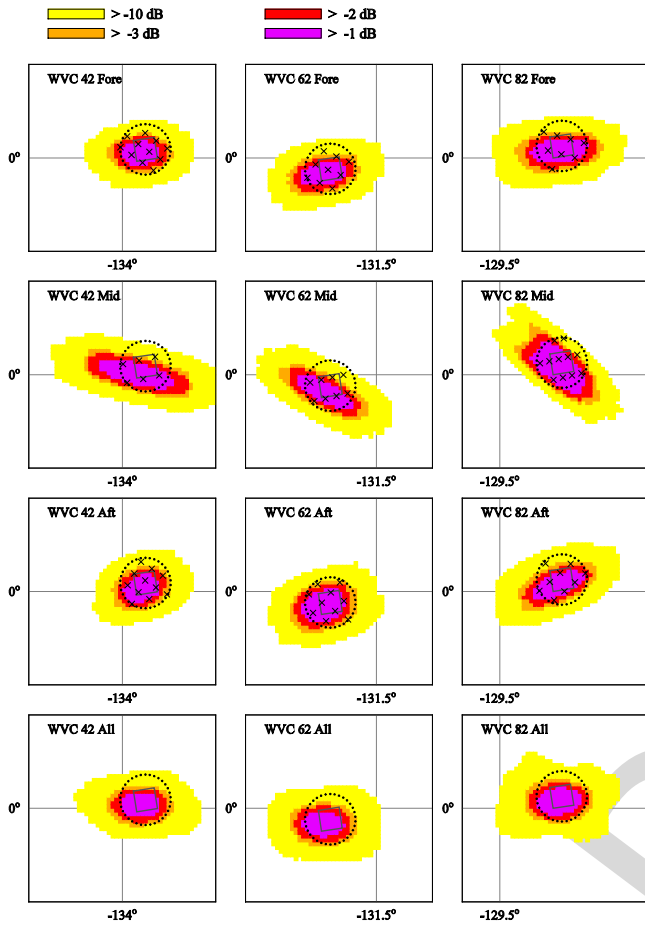


Fig. 3. Cumulative spatial response functions for ASCAT-6.25. The square box gives the WVC (size 6.25 km) and the dotted circle the boundary of the aggregation area (radius 7.5 km).

the bottom row of panels shows the CSRf of all three beams. In this case, the  $-3$  dB contour follows the aggregation area boundary less well, notably for the mid beam. The CSRfs have an elliptical shape, reflecting the shape of the contributing SRFs, notably for the mid beam at low incidence. A considerable portion of the CSRf may lie outside the aggregation area, and the difference in shape indicates poor overlap between the three beams. The CSRfs of all three beams (bottom row of panels in Fig. 3) are more circular, though for the three WVCs shown, it is located slightly southward of the aggregation area.

The true spatial resolution may be characterized by calculating the area of the CSRf enclosed by the  $-3$  dB contour. Fig. 4 shows that the area as a function of incidence angle for various values of the aggregation radius  $R$ . Fig. 4 shows results for the fore, mid, and aft beams separately, and for all beams together. The  $-3$  dB area varies slightly with the incidence angle, due to the varying shape and size of the SRFs over the swath. Note that the all-beam  $-3$  dB area (lower right panel of Fig. 4) is nearly constant with the incidence angle. Approximating the all-beam  $-3$  dB area by a circle and taking its diameter as a measure of the true spatial resolution (this is the full-width half-maximum measure), one arrives at 28 km for  $R = 15$  km (ASCAT-coastal), 20 km for  $R = 10$  km, 17 km for  $R = 7.5$  km, and 14 km for

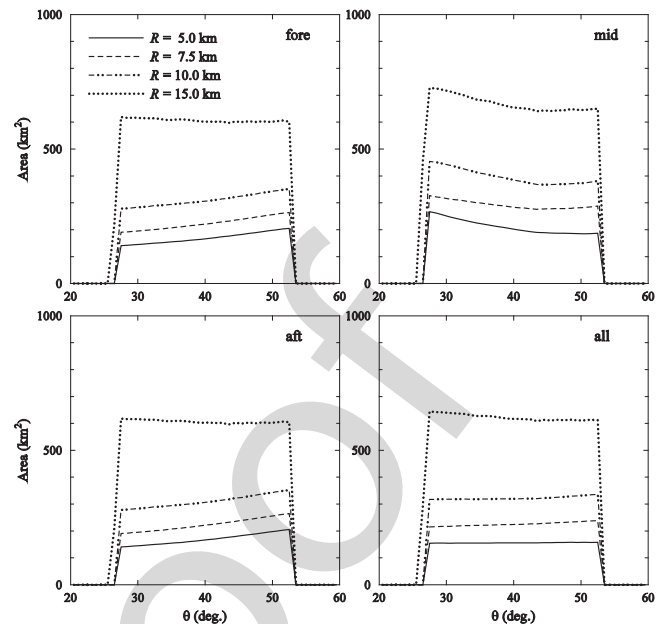


Fig. 4. Area within the  $-3$  dB CSRf contour versus incidence angle for ASCAT-6.25 at various aggregation radii for the fore, mid, and aft beams separately and for all beams together.

$R = 5$  km. Of course, the size of the SRFs poses a lower limit on the true spatial resolution defined this way.

Figs. 2 and 3 indicate that the overlap between the three beams gets worse as  $R$  decreases. Additionally, Fig. 4 gives some indication in that direction, as the area for all beams at  $R = 5.0$  km is smaller than the area of each individual beam. The overlap  $O_{\alpha\beta}$  between the CSRfs for beams  $\alpha$  and  $\beta$  can be quantified as

$$O_{\alpha\beta} = \frac{I_{\alpha\beta}^2}{I_{\alpha\alpha}I_{\beta\beta}} \quad (1)$$

with

$$I_{\alpha\beta} = \iint d\lambda d\phi \cos \phi C_{\alpha}(\lambda, \phi) C_{\beta}(\lambda, \phi) \quad (2)$$

where  $C_{\alpha}$  stands for the CSRf of beam  $\alpha$  as a function of geographical longitude  $\lambda$  and latitude  $\phi$ , and the integration is over the entire domain of the CSRfs. From (1) and (2), it is clear that the overlap  $O_{\alpha\beta}$  defined in this way equals one if the two CSRfs are identical and zero if they are disjunct.

Fig. 5 shows the overlap as a function of incidence angle for various aggregation radii. The overlap between the fore and the aft beam is very good and degrades only slightly with decreasing  $R$ . Figs. 2 and 3 show that this is due to the fact that the CSRf of each beam is elliptical, and that the ellipses have about the same orientation for the fore and aft beam. The CSRf ellipse of the mid beam makes an angle with that of the fore or aft beam, and indeed Fig. 5 shows poorer overlap between the mid and fore beams and between the mid and aft beams. As the CSRfs become more elliptical with decreasing  $R$ , the overlap of the fore or aft beam with the mid beam rapidly decreases with  $R$ . The  $-3$  dB CSRf areas

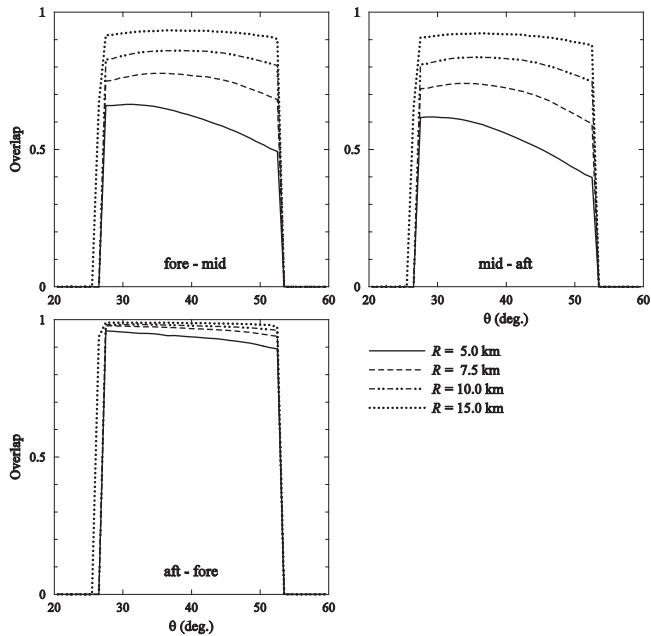


Fig. 5. Overlap between the three possible beam pairs versus incidence angle for ASCAT-6.25 at various aggregation radii.

TABLE I  
BUOY COMPARISON FOR AUGUST 2013

$R$ (km)	$\sigma_s$ (m/s)	$\sigma_d$ (deg)	$\sigma_l$ (m/s)	$\sigma_t$ (m/s)
5.0	1.01	17.9	1.70	1.42
7.5	0.99	16.6	1.64	1.39
10.0	0.98	16.9	1.61	1.37
15.0	0.98	16.8	1.59	1.36
Accuracy	0.02	0.3	0.03	0.03

and overlaps show no significant dependency on geographical latitude.

#### IV. ACCURACY

##### A. Buoy Comparison

Table I shows the standard deviations of the differences between scatterometer and buoy winds for wind speed, wind direction, wind component in the along-track direction  $l$ , and wind component in the cross-track direction  $t$ , for various values of the aggregation radius,  $R$ . The results in Table I are based on all available data from August 2013. Only collocations common to all values of  $R$  were taken into account, resulting in 2682 collocations. Wind direction statistics are based on a smaller number of collocations (between 1892 and 1907, depending on the value of  $R$ ), since these were only calculated for wind speeds exceeding 4 m/s. The accuracies in the last row of Table I are estimates based on the inverse square root of the number of collocations.

Table I shows that in general the differences between scatterometer and buoy winds tend to increase with decreasing

$R$ . However, the differences are hardly significant, except for  $R = 5$  km. Here, the differences are clearly larger, notably for the wind direction and the wind components.

##### B. Triple Collocation

Given three collocated datasets, triple collocation analysis allows to calculate the linear calibration coefficients of two sets relative to the third (reference) one and to retrieve the error in each dataset, provided that linear calibration is sufficient and that the errors are constant and independent [12], [13]. Table II shows the triple collocation results for August 2013 as a function of averaging radius  $R$ . It lists the error standard deviations for  $l$  and  $t$ ,  $\sigma_l$  and  $\sigma_t$ , the number of collocations used to arrive at the error estimates  $N$ , and the representativeness error variances obtained from the spatial variances at a scale of 200 km (see Section IV-C)  $r_l^2$  and  $r_t^2$ . The standard deviations of the errors in Table II are with respect to the scales resolved by the scatterometer, so the representativeness error is incorporated in the background error. The triple collocation analysis used only collocations that are common to all values of  $R$ . The last row gives the accuracy of the errors estimated under the assumption that the errors are Gaussian [13].

Table II shows that within the estimated accuracy, the buoy errors and the background errors do not depend on of the averaging radius, while the scatterometer errors increase with decreasing  $R$ , though the increase is only significant between  $R = 15$  km and  $R = 5$  km. The buoy errors are the same for  $l$  and  $t$ , whereas the scatterometer and background errors are larger for  $l$  than for  $t$ . The representativeness errors  $r_l^2$  and  $r_t^2$  increase with the decreasing value of  $R$ , indicating that indeed the scatterometer winds contain more detail than the ECMWF background winds. As stated at the beginning of this chapter, the background error estimates are for ECMWF forecasts on a 70 km grid.

##### C. Spatial Variance Error Model

The previous results suggest that decreasing the aggregation radius leads to higher spatial resolution, but also to more noise (larger errors) in the ASCAT-6.25 wind product. A common approach to such questions is spectral analysis. Fig. 6 shows the ASCAT-6.25 spectra for the wind components  $l$  (left-hand panel) and  $t$  (right-hand panel) for various values of the aggregation radius  $R$ . The spectra show a bump at high wavenumbers that increases as  $R$  decreases. This bump was previously observed in the spectra of the ASCAT-coastal product, but its exact origin was not clear. It is argued below that this is caused by correlated noise.

One problem in the interpretation of spectra like those in Fig. 6 is that they show the variance density in the wavenumber domain, but that this cannot be translated to the spatial domain in terms of spatial scales. Therefore, Vogelzang *et al.* [14] introduced a statistic called spatial variance. It is the cumulative variance as a function of scale (or sample length).

For a discrete equidistant dataset  $\{u_i\} = \{u(r_i)\}$  with  $r_i = i\Delta r$ ,  $i = 1, 2, \dots, N$ , the first and second moments for a sample

TABLE II  
TRIPLE COLLOCATION RESULTS FOR AUGUST 2013

$R$ (km)	Buoys		Scatterometer		Background		$N$	$r_l^2$ (m <sup>2</sup> /s <sup>2</sup> )	$r_t^2$ (m <sup>2</sup> /s <sup>2</sup> )
	$\sigma_l$ (m/s)	$\sigma_t$ (m/s)	$\sigma_l$ (m/s)	$\sigma_t$ (m/s)	$\sigma_l$ (m/s)	$\sigma_t$ (m/s)			
5.0	0.97	1.02	1.23	0.80	1.40	1.24	2655	1.10	1.37
7.5	1.00	1.02	1.11	0.74	1.39	1.22	2653	0.87	1.11
10.0	1.02	1.03	1.08	0.68	1.39	1.24	2655	0.75	0.97
15.0	1.01	1.04	1.02	0.65	1.40	1.21	2652	0.64	0.83
Accuracy	0.08	0.08	0.08	0.06	0.05	0.03			

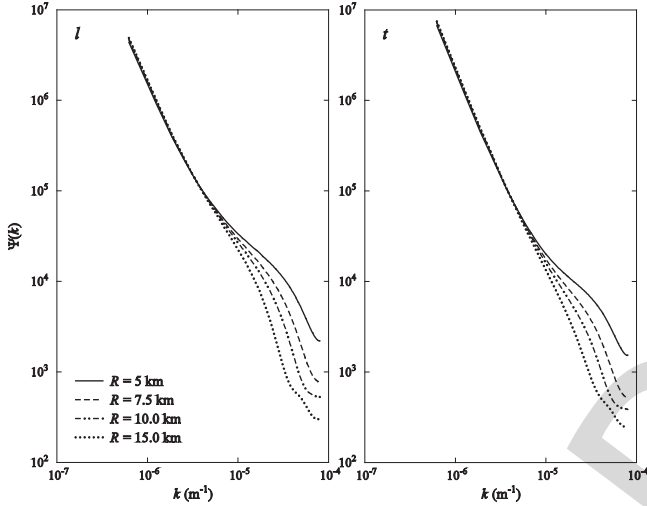


Fig. 6. ASCAT-6.25 spectra for the along-track and cross-track wind components at various aggregation radii.

of length  $n + 1$  (scale  $r_n = n\Delta r$  and lag  $n$ , where the lag is defined as the distance between two data points in units of the grid size) starting at a certain point  $u_i$  are defined as

$$M_1(i, n) = \frac{1}{n+1} \sum_{j=0}^n u_{i+j}, \quad M_2(i, n) = \frac{1}{n+1} \sum_{j=0}^n u_{i+j}^2. \quad (3)$$

The spatial variance is defined as the average variance of all samples with length  $n + 1$

$$V(n) = \langle M_2(i, n) - M_1^2(i, n) \rangle \quad (4)$$

where the brackets  $\langle \rangle$  denote averaging over all available samples, each sample being characterized by  $i$ , the index of its starting point. Its discrete derivative is defined as

$$\Delta V(n) = \frac{V(n) - V(n-1)}{\Delta r} \quad (5)$$

with  $V(0) = 0$ . The samples can be taken in the along-track direction, as in [14], but also in the cross-track direction, though the maximum lag size in that direction is limited by the swath width of 81 WVCs at each side of the satellite track for ASCAT-6.25.

Since the spatial variance  $V(n)$  is the cumulative variance contained in scales up to  $r_n$ , its derivative  $\Delta V(n)$  is the inc-

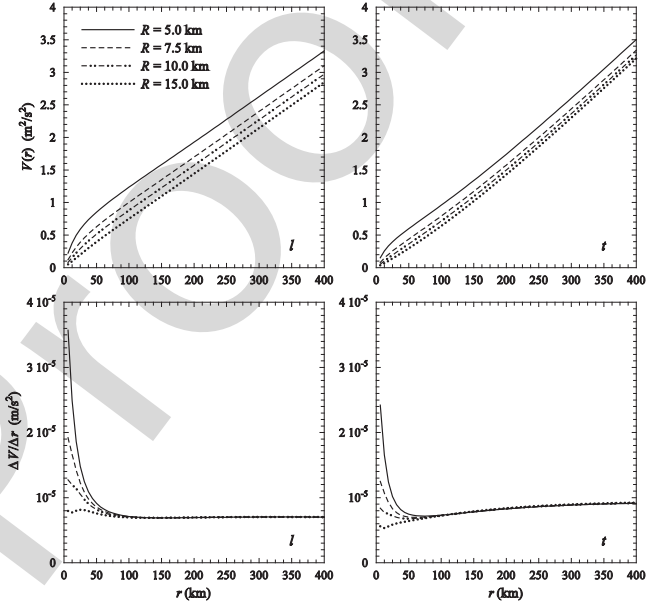


Fig. 7. ASCAT-6.25 spatial variance (top panels) and its derivative (bottom panels) for the wind components  $l$  (left-hand panels) and  $t$  (right-hand panels) at various aggregation radii.

crease in variance when going from scale  $r_{n-1}$  to  $r_n$  and can therefore be interpreted as a variance density. The difference between the spatial variances of scatterometer and background at a scale of 200 km is a good measure of the representativeness error. It has been used in the triple collocation analysis presented in Section IV-B.

Fig. 7 shows the along-track sampled spatial variances for the ASCAT-6.25 wind components  $l$  and  $t$  (top left and top right panels, respectively) as well as their discrete derivative (bottom left and bottom right panels). Fig. 7 shows that  $V$  increases rapidly for scales below 100 km, notably for small values of  $R$ . This behavior is seen more clearly in the plots of  $\Delta V$ : at small lags, a peak is visible that gets higher as  $R$  gets smaller. For  $R = 15$  km (oversampled ASCAT-coastal), the peak has almost disappeared. The peak has its maximum at the first lag, so increase in noise with decreasing  $R$  seems a plausible explanation for it. Since the aggregation areas of neighboring WVCs overlap, also at  $R = 5$  km, the noise must be correlated.

TABLE III  
SPATIAL VARIANCE ERROR ANALYSIS RESULTS FOR THE ALONG-TRACK  
SAMPLED  $l$  COMPONENT OF ASCAT-6.25 WITH  $R = 5$  km AS A FUNCTION  
OF  $J$

$J$	$\sigma^2$	$\rho_1$	$\rho_2$	$\rho_3$	$\rho_4$	$\rho_5$	$\rho_6$
1	0.347	0	0	0	0	0	0
2	0.571	0.392	0	0	0	0	0
3	0.598	0.420	0.045	0	0	0	0
4	0.571	0.393	0.000	-0.047	0	0	0
5	0.547	0.367	-0.044	-0.093	-0.044	0	0
6	0.532	0.348	-0.073	-0.124	-0.074	-0.028	0
7	0.522	0.335	-0.095	-0.147	-0.095	-0.049	-0.020

TABLE IV  
SPATIAL VARIANCE ERROR ANALYSIS RESULTS FOR AUGUST 2013

Sampling type	$R$ (km)	$l$			$t$		
		$\sigma^2$ ( $\text{m}^2/\text{s}^2$ )	$\rho_1$	$\rho_2$	$\sigma^2$ ( $\text{m}^2/\text{s}^2$ )	$\rho_1$	$\rho_2$
Along track	5.0	0.60	0.42	0.05	0.39	0.40	0.04
	7.5	0.33	0.57	0.13	0.20	0.56	0.11
	10.0	0.17	0.66	0.23	0.10	0.65	0.23
Cross track	5.0	0.51	0.23	0.01	0.38	0.25	0.01
	7.5	0.26	0.47	0.06	0.19	0.49	0.07
	10.0	0.14	0.60	0.23	0.10	0.62	0.24

The spatial variance is a linear combination of the second-order structure function at various distances, which in turn is the Fourier transform of the spectrum [14], see also the Appendix. Therefore, the change in the spectral shape with  $R$  in Fig. 6 is attributed to correlated noise. Note that uncorrelated (white) noise would lead to a constant noise floor.

This interpretation of Figs. 6 and 7 is supported by experiments with simulated data, a few examples of which are presented in the Appendix. There it is also shown that if the noise contribution can be isolated, so  $\Delta V = \Delta V^{(S)} + \Delta V^{(N)}$ , it is possible to calculate the noise variance and its correlation coefficients. The bottom panels of Fig. 7 suggest to take  $\Delta V$  for  $R = 15$  km as  $\Delta V^{(S)}$ , since here almost no noise peak is visible. Application of the spatial variance error model from the Appendix thus yields results with respect to the ASCAT-coastal product. The number of correlation coefficients involved must be determined *a posteriori* as follows. As an example, Table III gives the results for the along-track sampled wind component  $l$  of ASCAT-6.25 with  $R = 5$  km as a function of  $J$  the number of lags taken into account. For  $J = 1$ , only the variance  $\sigma^2$  can be retrieved; for  $J > 1$ , also  $J - 1$  correlations can be found. The highest variance,  $\sigma^2 = 0.598 \text{ m}^2/\text{s}^2$  is found for  $J = 3$ . Here, positive correlations are found at lags 1 and 2 (neighbors and next-neighbors). For higher values of  $J$ , the additional correlation coefficients become small and negative, indicating that the  $J = 3$  results are the most reliable. Moreover, from geometrical considerations, one does not expect correlations from lag 3 or higher.

Table IV shows the results for the excess variance and its correlations with respect to  $R = 15$  km as a function of  $R$

TABLE V  
EXCESS VARIANCES W.R.T. 15 KM AVERAGING RADIUS FROM TRIPLE  
COLLOCATION (TC) AND SPATIAL VARIANCE ANALYSIS (SV)

$R$ (km)	$\Delta\sigma_l^2$ ( $\text{m}^2/\text{s}^2$ )		$\Delta\sigma_t^2$ ( $\text{m}^2/\text{s}^2$ )	
	TC	SV	TC	SV
5.0	0.52	0.60	0.25	0.39
7.5	0.21	0.33	0.14	0.30
10.0	0.10	0.17	0.06	0.10

for the wind components  $l$  and  $t$ . The excess variance increases with decreasing  $R$  for both  $l$  and  $t$ , and for both along-track and cross-track sampling, while the correlation coefficients decrease. This is consistent with the notion that smaller aggregation areas lead to noisier radar cross sections and also to less overlap between the CSRFs of the beams (see Fig. 5). For the along-track wind component  $l$ , the error model yields slightly higher excess noise variances with along-track sampled spatial variances than with cross-track sampled ones, while for the cross-track wind component  $t$  both sampling types give very similar results. The correlation coefficients show a clear dependency on the sampling type, caused by different overlaps of the CSRFs (see Figs. 1 and 3). They are remarkably similar for  $l$  and  $t$ .

#### D. Comparison

The spatial variance error analysis shows a considerable increase in noise w.r.t. the ASCAT coastal product when going to a smaller averaging radius. This is confirmed by the buoy comparison and the triple collocation analysis, but only significantly between  $R = 15$  km and  $R = 5$  km.

The accuracy of the spatial variance error model results is hard to estimate. It depends not only on the statistical accuracy of the spatial variances themselves, but also on the relation between spatial variances and second-order structure functions, which becomes approximate when the dataset contains missing points and the sampling strategy may become important. However, sampling effects on the error model are expected to be small, because the noise contribution is obtained by subtracting a reference spatial variance that has been sampled in the same way. An error of about  $0.05 \text{ m}^2/\text{s}^2$  in the error variance therefore seems reasonable. It leads to consistent results in Table IV and is in agreement with the accuracies estimated from triple collocation. The spatial variance analysis assumes that the signal content of the various wind products is independent of the averaging radius. When going to smaller averaging radius, one expects the effective resolution to improve and thus the signal content at small distances to increase. Therefore, the spatial variance analysis may overestimate the errors because its reference level is too low.

Table V gives the excess variances calculated from the triple collocation results (by taking the values for  $R = 15$  km from Table III as reference, labeled TC) and from the spatial variance analysis (from Table IV, labeled SV). The spatial variance

analysis indeed yields slightly higher values for the excess variance than the triple collocation analysis, but the difference is small and hardly significant because of the limited accuracy of the triple collocation results. Moreover, the spatial variance analysis covers all Earth, while the triple collocation analysis is restricted to the buoy locations. Nevertheless, these results indicate that both methods give consistent results.

## V. STATISTICAL CONSISTENCY

The normalized inversion residual, MLE, can be converted to an *a priori* probability  $p$ , that an ambiguous solution returned by the inversion algorithm is the correct solution. This can be verified after ambiguity removal by calculating  $P(\text{sel}|p)$ , the probability that a solution is selected given its *a priori* probability. Fig. 8 shows the probability density function (pdf) of  $P(\text{sel}|p)$  against  $p$  for ASCAT-6.25 with 7.5 km aggregation radius (solid curve) and for ASCAT-coastal (dashed curve). In case of perfect statistical consistency, the pdf of  $P(\text{sel}|p)$  would increase linearly from value zero at  $p = 0$  to value two at  $p = 1$  (so that the integrated pdf equals one), as indicated by the dotted line in Fig. 8.

The overall statistical consistency is quite good, but  $P(\text{sel}|p)$  is slightly too high for low values of  $p$  and slightly too low for high values of  $p$ . This deviation from perfect statistical consistency is stronger for ASCAT-6.25 than for ASCAT-coastal. This means that the 2DVAR ambiguity removal scheme selects too many ambiguities with low *a priori* probability and too few with high probability. Apparently, 2DVAR puts too much weight on spatial consistency at the cost of statistical consistency. This might be improved by tuning the 2DVAR parameters, but that is outside the scope of this study.

## VI. DISCUSSION

The results in Section III show that the  $-3$  dB area of the all-beam CSRF varies with aggregation radius  $R$  from more than  $600 \text{ km}^2$  for  $R = 15 \text{ km}$  (ASCAT-coastal) to about  $150 \text{ km}^2$  for  $R = 5 \text{ km}$ . Assuming a circular shape for the CSRF, the true spatial resolution is defined as the diameter of this circle. It is about  $28 \text{ km}$  for ASCAT-coastal and about  $20 \text{ km}$  for  $R = 10 \text{ km}$ ,  $17 \text{ km}$  for  $R = 7.5 \text{ km}$ , and  $14 \text{ km}$  for  $R = 5 \text{ km}$ . Though the ASCAT-6.25 CSRF for  $R = 7.5 \text{ km}$  is elliptical in shape rather than circular, Fig. 3 shows that a true spatial resolution of about  $17 \text{ km}$  is indeed a good estimate.

The results in Section IV show that ASCAT-6.25 wind products with an averaging radius smaller than  $15 \text{ km}$  contain more noise than ASCAT-coastal, as identified by buoy comparison, triple collocation, and spatial variance analysis. The noise increases rapidly with decreasing  $R$ .

An aggregation radius of  $7.5 \text{ km}$ , half of that for the ASCAT-coastal product, is a good compromise between wind quality and spatial resolution: it yields a true spatial resolution of about  $17 \text{ km}$ , clearly better than the  $28 \text{ km}$  for ASCAT-coastal, while the excess noise variance (relative to ASCAT coastal) is only  $0.2 \text{ m}^2/\text{s}^2$ . This value is therefore adopted as default in AWDP, though it is under user control with a command line argument.

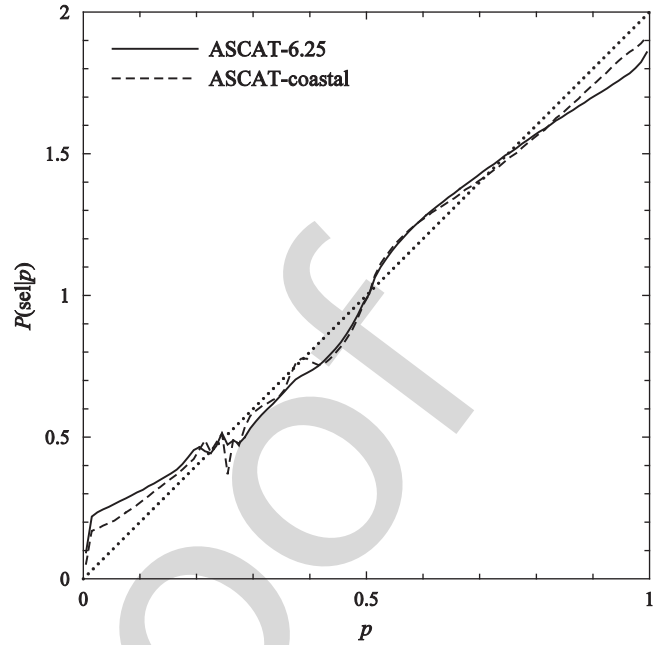


Fig. 8. Statistical consistency for ASCAT-6.25 at 7.5 km aggregation radius and ASCAT-coastal.

Fig. 3 also shows that for the default ASCAT-6.25 the contributing SRFs may not be divided evenly over the aggregation area, causing the CSRF to be shifted with respect to the WVC centre. This adds to the poor overlap between the CSRFs of the three beams, see Fig. 5, which, in turn, leads to geophysical errors because different beams sample different parts of the ocean surface. This is in particular unwanted in dynamic areas—just the type of situation where high-resolution wind fields are of interest. Such detrimental effects can be mitigated by optimizing the SRF sampling using a WVC grid synchronized to the mid-beam antenna pattern. This approach is beyond the scope of this paper, but is discussed further in [15]. The statistical consistency of ASCAT-6.25 with 7.5 km aggregation radius is slightly worse than that of ASCAT-coastal. In principle, this could be improved by better tuning of the error variances in 2DVAR, but that is also considered outside the scope of this paper. Moreover, the degradation in statistical consistency is at an acceptable level and must be balanced against a better true spatial resolution.

Despite its nonoptimal SRF sampling, ASCAT-6.25 clearly has added value compared to ASCAT-coastal: it is capable of detecting smaller features as the cost of slightly more noise. As an example, Fig. 9 shows von Kármán vortices in the wake of Madeira recorded August 4, 2013, for ASCAT-coastal (top panel) and ASCAT-6.25 (bottom panel). Though the vortices are recognizable in ASCAT-coastal, they show more detail in ASCAT-6.25.

At this moment, the OSI SAF has no plans to disseminate a near real-time ASCAT-6.25 product, so interested users have to do their own processing. This may be reconsidered in case of sufficient user demand.

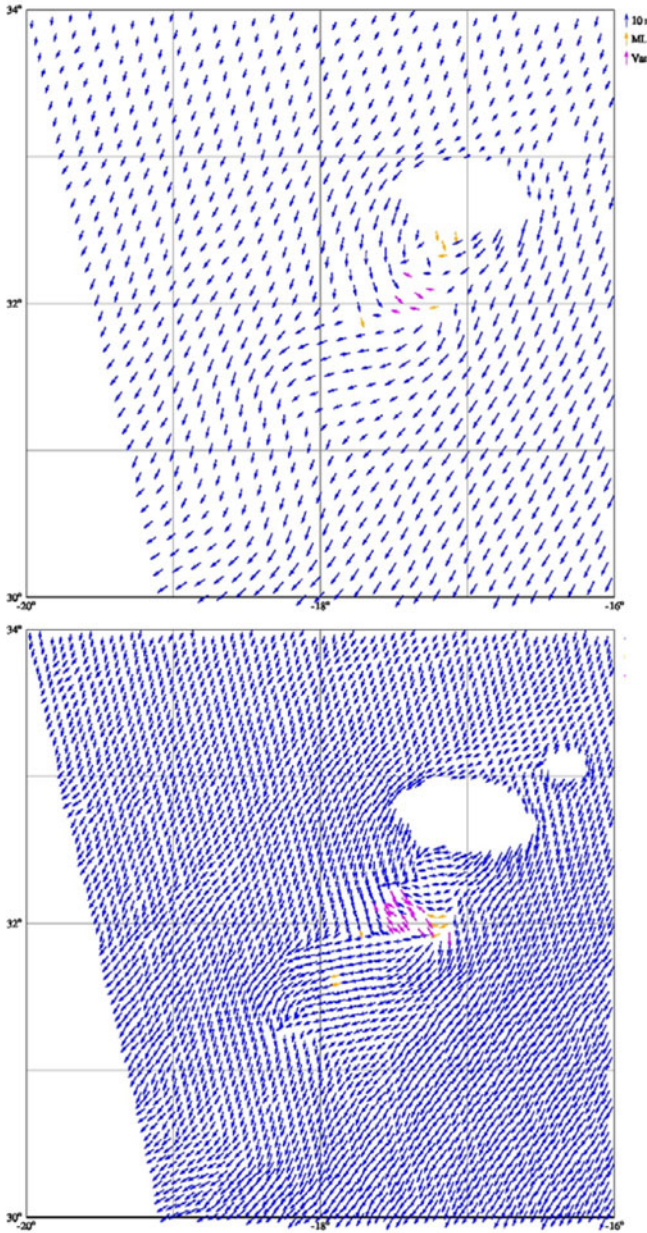


Fig. 9. ASCAT-coastal (top panel) and ASCAT-6.25 (bottom panel) wind field on August 4, 2013 at about 22:00 showing von Kármán vortices southwest of the isle of Madeira. The isle reveals itself as the area of missing wind vectors south of 33 °N, -17 °E).

## VII. CONCLUSION

From version 2.4 onward, the AWDP is able to process full-resolution L1B radar cross-section data to a wind product on a 6.25 km grid. The aggregation radius  $R$  is the crucial parameter. A value of 7.5 km, half of that for ASCAT-coastal, yields the best compromise between spatial resolution and wind accuracy and is chosen as default value in AWDP. Taking the -3 dB contour of the CSRF as a measure for the true spatial resolution, the ASCAT-6.25 resolution is about 17 km, better than the 28 km of ASCAT-coastal. Buoy comparison, triple collocation, and spatial variance analysis show that the default ASCAT-6.25 product also contains slightly more noise ( $0.2 \text{ m}^2/\text{s}^2$  more vari-

ance in the wind components) than the ASCAT-coastal product. This is due to the fact that less SRFs contribute to the CSRF, notably for the mid beam at small incidence angles. This leads to more noise in the average radar cross sections and, hence, in the retrieved winds. Also the overlap between the CSRFs of the three beams is poorer for ASCAT-6.25 than for ASCAT-coastal, leading to larger geophysical noise. Nevertheless, the ASCAT-6.25 wind product is valuable in studying dynamical mesoscale features like convection cells, coastal jets, and von Kármán vortices.

## APPENDIX SPATIAL VARIANCE ERROR ANALYSIS

Suppose we have a dataset  $\{u_i\} = \{u(r_i)\}$  with  $r_i = i\Delta r$ ,  $i = 0, 1, \dots, n$ . Suppose further that the data contain noise, so that  $u_i = s_i + \varepsilon_i$  with  $s_i$  the pure signal and  $\varepsilon_i$  the noise. The increment at lag  $j$ ,  $\delta_{i,j} = u_i - u_{i+j}$ , can be split into a signal part and a noise part as

$$\delta_{i,j} = (s_i - s_{i+j}) + (\varepsilon_i - \varepsilon_{i+j}). \quad (\text{A.1})$$

The second-order structure function at lag  $j$  is defined as

$$D_j = \langle \delta_{i,j}^2 \rangle \quad (\text{A.2})$$

where the brackets  $\langle \rangle$  denote averaging over all samples in the dataset. Assuming that the noise is not correlated with the signal strength, so  $\langle (s_i - s_{i+j})(\varepsilon_i - \varepsilon_{i+j}) \rangle = 0$ , the structure function can also be written as the sum of a signal part  $D_j^{(S)}$  and a noise part,  $D_j^{(N)}$ , with

$$D_j^{(S)} = \langle (s_i - s_{i+j})^2 \rangle, \quad (\text{A.3})$$

$$D_j^{(N)} = \langle (\varepsilon_i - \varepsilon_{i+j})^2 \rangle = 2\sigma^2(1 - \rho_j) \quad (\text{A.4})$$

where  $\sigma^2 = \langle \varepsilon_i^2 \rangle = \langle \varepsilon_{i+j}^2 \rangle$  is the noise variance and  $\rho_j = \langle \varepsilon_i \varepsilon_{i+j} \rangle$  the noise autocorrelation. The spatial variance  $V_j$  is defined in [9]. It is related to the second-order structure function by the Yates relation [16]

$$V_j = \frac{1}{(j+1)^2} \sum_{k=1}^j (j+1-k) D_k. \quad (\text{A.5})$$

Since the relation between spatial variance and second-order structure function is linear, also the spatial variance can be split in a signal part and a noise part,  $V_j = V_j^{(S)} + V_j^{(N)}$ , with

$$V_j^{(S)} = \frac{1}{(j+1)^2} \sum_{k=1}^j (j+1-k) D_k^{(S)}, \quad (\text{A.6})$$

$$V_j^{(N)} = \frac{2\sigma^2}{(j+1)^2} \sum_{k=1}^j (j+1-k) (1 - \rho_k). \quad (\text{A.7})$$

The effect of noise is most clearly exhibited by the discrete derivative of the spatial variance,

$$\Delta V_j = \frac{V_j - V_{j-1}}{\Delta r} \quad (\text{A.8})$$

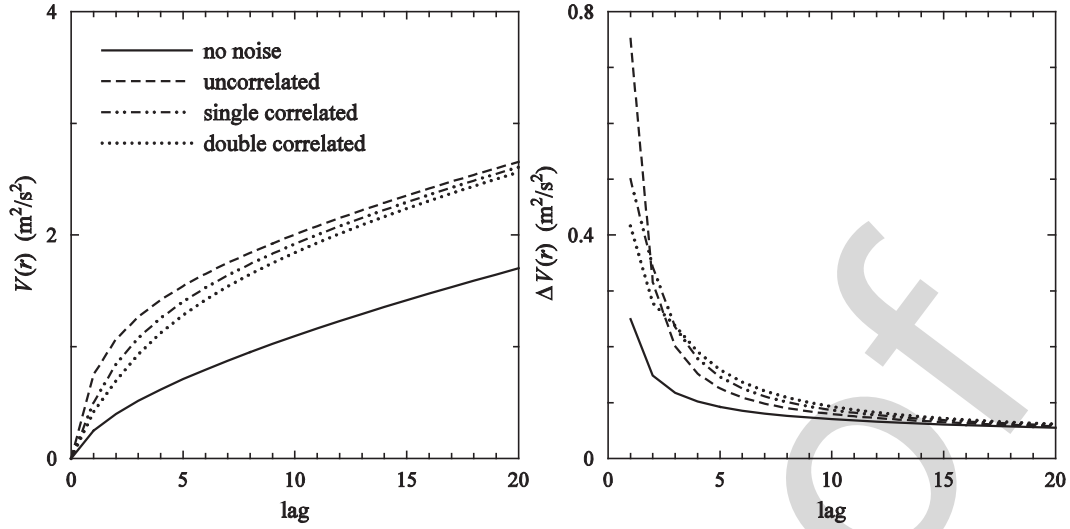


Fig. A1. Spatial variance (left-hand panel) and its derivative (right-hand panel) as a function of lag size for a fractional Brownian motion process with exponent  $2/3$  without noise (solid curves), uncorrelated noise (dashed curves), single correlated noise (dotted–dotted–dashed curves) and double correlated noise (dotted curves).

TABLE A1  
ERROR ANALYSIS RESULTS FOR FRACTIONAL BROWNIAN MOTION WITH  
CORRELATED GAUSSIAN NOISE

J	$\sigma^2$	$\rho_1$	$\rho_2$	$\rho_3$	$\rho_4$	$\rho_5$
1	0.199	0	0	0	0	0
2	0.398	0.498	0	0	0	0
3	0.596	0.665	0.333	0	0	0
4	0.795	0.749	0.500	0.250	0	0
5	0.995	0.800	0.600	0.401	0.201	0
6	0.995	0.800	0.600	0.401	0.201	0.00005
Exact	1.0	0.8	0.6	0.4	0.2	0.0

with  $j > 0$  and  $V_0 = 0$ .  $\Delta V_j$  is the increase in variance when going from scale  $r_{j-1}$  to  $r_j$ . From the foregoing, it is clear that it too can be split in a signal part and a noise part. From (A.7) and (A.8), one obtains for the noise part

$$\Delta V_j^{(N)} = \frac{\sigma^2}{\Delta r} \sum_{k=1}^j 2^k \frac{(2j+1) - j(j-1)}{j^2(j+1)^2} (1 - \rho_k). \quad (\text{A.9})$$

If the noise is uncorrelated, i.e.,  $\rho_k = 0$  for all  $k$ , (A.9) reduces to

$$\Delta V_j^{(N)} = \frac{\sigma^2}{\Delta r} \frac{1}{j(j+1)}. \quad (\text{A.10})$$

In this case,  $\Delta V_j^{(N)}$  peaks at lag 1 and the peak height drops quadratically with the lag number. For correlated noise, the peak may become lower and shifted to higher lag numbers, depending on the nature of the correlations.

As an example, Fig. A1 shows  $V_j$  and  $\Delta V_j$  against lag number  $j$  for a fractional Brownian motion (FBM) process with exponent  $2/3$  and unit grid size. The solid curve is without noise. Its second-order structure function has a  $2/3$  power law behavior, and so has its spatial variance [13]. The derivative of the spatial variance, therefore, follows a power law with exponent  $-1/3$  which causes in this case a peak at low lag numbers. The dashed curves are with uncorrelated Gaussian noise of unit variance.

Now the noise peak at low lag numbers is clearly visible. When the noise is correlated with neighbors (dotted–dotted–dashed curves) and next-neighbors (dotted curves) the noise peak get lower and broader.

Equation (A.9) can be written in compact form as

$$\Delta V_j^{(N)} = \frac{\sigma^2}{\Delta r} \sum_{k=1}^j C_{jk} R_k \quad (\text{A.11})$$

with  $R_k = 1 - \rho_k$  and

$$C_{jk} = \begin{cases} 2^{k(2j+1) - j(j-1)} / j^2(j+1)^2, & k \leq j \\ 0, & k > j \end{cases}. \quad (\text{A.12})$$

Suppose we have values of  $\Delta V_j^{(N)}$  for  $j = 1, 2, \dots, J$ . Equation (A.11) defines a system of  $J$  equations with  $J+1$  unknowns  $R_j$ ,  $j = 1, 2, \dots, J$  and  $\sigma^2$ . This system can be solved under the assumption that the correlation coefficient becomes zero for lag  $J$ , so  $R_J = 1 - \rho_J = 1$ . This assumption can be tested afterward by varying  $J$ .

To cast (A.11) in a form more suitable for solution, first divide all equations by  $\Delta V_1^{(N)}$  to eliminate  $\sigma^2$  and  $\Delta r$

$$\frac{\Delta V_j^{(N)}}{\Delta V_1^{(N)}} = \sum_{k=1}^j C_{jk} \frac{R_k}{C_{11} R_1}, \quad j = 2, 3, \dots, J. \quad (\text{A.13})$$

Multiplying with  $C_{11} R_1$ , rearranging terms, and introducing  $\Delta_j = \Delta V_j^{(N)} / \Delta V_1^{(N)}$  yields

$$-C_{11} \Delta_j R_1 + \sum_{k=1}^j C_{jk} R_k = 0, \quad j = 2, 3, \dots, J. \quad (\text{A.14})$$

Since  $R_J = 1$  this is a system of  $J-1$  equations with  $J-1$  unknowns. This system is easily triangularized and solved. The variance can then be retrieved from (A.11) for  $j = 1$  as

$$\sigma^2 = \frac{\Delta r \Delta V_1^{(N)}}{C_{11} R_1}. \quad (\text{A.15})$$

The procedure outlined above has been tested on a dataset containing  $2^{20}$  values from a FBM process with exponent  $2/3$ . Gaussian noise of unit variance was added to it, and the noise was made correlated using a running average so that  $\rho_1$  to  $\rho_4$  have values 0.8, 0.6, 0.4, and 0.2, respectively. The results for  $J$  running from 1 to 6 are shown in Table A1. The table shows that the variance and the correlation coefficients converge to their exact values shown in the bottom row as  $J$  increases to 5. The value of  $\sigma^2$  is retrieved with an accuracy of about 0.005, those of the correlation coefficients with an accuracy of about 0.001. This is of the order of the inverse square root of the number of points in the dataset. For  $J = 6$ , the excess correlation coefficient  $\rho_5$  is smaller than the accuracy, consistent with zero value. This holds also for higher correlation coefficients at higher values for  $J$ . Note that the variance is underestimated when an insufficient number of correlation coefficients is assumed ( $J < 5$ ).

#### ACKNOWLEDGMENT

The Fractional Brownian Motion data were kindly provided by G. P. King (ICM, Barcelona, Spain) using the free MATLAB code developed by A. Holtsberg. The authors wish to thank J. Bidlot (ECMWF) for his assistance in obtaining buoy measurements.

#### REFERENCES

- [1] J. Sienkiewicz *et al.*, "Impact of the loss of QuikSCAT on NOAA MWS marine warning and forecast operations," presented at the First International Ocean Vector Winds Science Team Meeting, Barcelona, Spain, May 2010. [Online]. Available: [http://coaps.fsu.edu/scatterometry/meeting/past.php#2010\\_may](http://coaps.fsu.edu/scatterometry/meeting/past.php#2010_may)
- [2] M. Bourassa *et al.*, "Remotely sensed winds and wind stresses for marine forecasting and ocean modeling," in *Proc. OceanObs09 Sustained Ocean Observ. Inf. Soc.*, 2010, vol. 2, doi:10.5270/OceanObs09.cwp.08.
- [3] J. Figa-Saldaña, J. Wilson, E. Attema, R. Gelsthorpe, M. Drinkwater, and A. Stoffelen, "The advanced scatterometer (ASCAT) on the meteorological operational (MetOp) platform: A follow on for the European wind scatterometers," *Can. J. Remote Sens.*, vol. 28, pp. 404–412, 2002, doi:10.5589/m02-035.
- [4] *ASCAT Wind Product User Manual*, KNMI, De Bilt, The Netherlands, 2013. [Online]. Available: [http://projects.knmi.nl/scatterometer/publications/pdf/ASCAT\\_Product\\_Manual.pdf](http://projects.knmi.nl/scatterometer/publications/pdf/ASCAT_Product_Manual.pdf)
- [5] A. Verhoef, M. Portabella, and A. Stoffelen, "High resolution ASCAT scatterometer winds near the coast," *IEEE Trans Geosci. Remote Sens.*, vol. 50, no. 7, pp. 2481–2487, Jul. 2012, doi:10.1109/TGRS.2011.2175001.
- [6] R. S. Dunbar *et al.*, *QuikSCAT Science Data Product User Manual, Version 3.0, JPL Document D-18053—Rev A*, Jet Propulsion Laboratory, Pasadena, CA, USA, Sep. 2006.
- [7] R. D. Lindsley, C. Anderson, J. Figa-Saldaña, and D. Long, "A parameterized ASCAT measurement spatial response function," *IEEE Trans. Geosci. Remote Sens.*, vol. 54, no. 8, pp. 4570–4579, Aug. 2016, doi:10.1109/TGRS.2016.2544835.
- [8] D. S. Early and D. G. Long, "Image reconstruction and enhanced resolution imaging from irregular samples," *IEEE Trans. Geosci. Remote Sens.*, vol. 39, no. 2, pp. 291–302, Feb. 2001, doi:10.1109/36.905237.
- [9] D. G. Long, P. Hardin, and P. Whiting, "Resolution enhancement of spaceborne scatterometer data," *IEEE Trans. Geosci. Remote Sens.*, vol. 31, no. 3, pp. 700–715, May 1993, doi:10.1109/36.225536.
- [10] R. Lindsley and D. G. Long, "Enhanced-resolution reconstruction of ASCAT backscatter measurements," *IEEE Trans. Geosci. Remote Sens.*, vol. 54, no. 5, pp. 2589–2601, May 2016, doi:10.1109/TGRS.2015.2503762.
- [11] R. D. Lindsley, J. R. Blodgett and D. G. Long, "Analysis and validation of high-resolution wind From ASCAT," *IEEE Trans. Geosci. Remote Sens.*, vol. 54, no. 10, pp. 5699–5711, Oct. 2016, doi:10.1109/TGRS.2016.2570245.
- [12] A. Stoffelen, "Toward the true near-surface wind speed: error modeling and calibration using triple collocation," *J. Geophys. Res.*, vol. 103, pp. 7755–7766, 1998.
- [13] J. Vogelzang, A. Stoffelen, A. Verhoef, and J. Figa-Saldaña, "On the quality of high-resolution scatterometer winds," *J. Geophys. Res.*, vol. 116, 2011, Art. no. C10033, doi:10.1029/2010JC006640.
- [14] J. Vogelzang, G. P. King, and A. Stoffelen, "Spatial variances of wind fields and their relation to second-order structure functions and spectra," *J. Geophys. Res. Oceans*, vol. 120, pp. 1048–1064, 2015, doi:10.1002/2014JC010239.
- [15] J. Vogelzang and A. Stoffelen, "ASCAT ultra high resolution wind products on optimised grids," *J. Sel. Topics Remote Sens.*, 2016, doi:10.1109/JSTARS.2016.2623861.
- [16] F. Yates, "Systematic sampling," *Philosoph. Trans. Roy. Soc.*, vol. A241, pp. 345–377, 1948, doi:10.1098/rsta.1948.0023.



**Jur Vogelzang** was born in 1955, in The Netherlands. He received the M.Sc. degree in theoretical physics from the Free University, Amsterdam, The Netherlands, in 1981, and the Ph.D. degree in physics on radar remote sensing from the University of Utrecht, Utrecht, The Netherlands, in 1998.

He is currently with the Royal Netherlands Meteorological Institute (KNMI), De Bilt, The Netherlands, where he is working on scatterometer wind products.



**Ad Stoffelen** was born in 1962, in The Netherlands. He received the M.Sc. degree in physics from the Technical University of Eindhoven, Eindhoven, The Netherlands, in 1987, and the Ph.D. degree in meteorology on scatterometry from the University of Utrecht, Utrecht, The Netherlands.

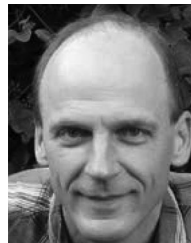
He currently leads a group on active satellite sensing at KNMI and is involved in topics from future missions and retrieval to 24/7 operations, user training and services. He is also deeply involved in the European Space Agency ADM-Aeolus Doppler Wind

Lidar mission.



**Richard D. Lindsley** (S'08–M'16) received the Ph.D. degree in electrical engineering from Brigham Young University (BYU), Provo, UT, USA, in 2015.

From 2008 to 2015, he was with the Microwave Earth Remote Sensing Laboratory, BYU. He is currently with the Remote Sensing Systems, Santa Rosa, CA, USA. His research interests include microwave remote sensing and signal processing.



**Anton Verhoef** was born in 1964, in The Netherlands. He received the M.Sc. degree in physics and the Ph.D. degree in solid state physics from the Rijksuniversiteit Groningen, Groningen, The Netherlands, in 1989 and 1994, respectively.

He is currently with the Royal Netherlands Meteorological Institute (KNMI), De Bilt, The Netherlands, and is working on scatterometry processing software development, data validation, quality monitoring, and user services.



**Jeroen Verspeek** was born in 1962, in The Netherlands. He received the M.Sc. degree in physics from the Technical University of Eindhoven, Eindhoven, The Netherlands, in 1988.

He is currently with the Royal Netherlands Meteorological Institute (KNMI), De Bilt, The Netherlands, and is working on scatterometer data interpretation, inversion, calibration, validation, and quality monitoring.

# The ASCAT 6.25-km Wind Product

Jur Vogelzang, Ad Stoffelen, Richard D. Lindsley, *Member, IEEE*, Anton Verhoef, and Jeroen Verspeek

**Abstract**—The advanced scatterometer (ASCAT) wind data processor (AWDP) produces ocean surface vector winds from radar measurements by the ASCAT on board the Metop satellites. So far, the ASCAT-coastal product with a grid size of 12.5 km has been the one with the highest resolution. Version 2.4 of AWDP, released May 2016, offers the possibility to process wind data on a 6.25 km grid. In this paper, the true spatial resolution and accuracy of that product is assessed using various methods. The crucial parameter is the radius of the area used to aggregate individual backscatter observations to a wind vector cell (WVC) level. A value of 7.5 km, half of that for ASCAT-coastal, appears to be the best compromise between resolution and accuracy. Spatial responses from multiple radar cross-section measurements are combined to cumulative responses, and show that the ASCAT-6.25 product has a spatial resolution of about 17 km, better than the 28 km found for the ASCAT-coastal product. The accuracy of the ASCAT-6.25 product is estimated using comparison with collocated buoys, triple collocation analysis, and a new method based on spatial variances. These methods show consistently that the ASCAT-6.25 product contains about  $0.2 \text{ m}^2/\text{s}^2$  more noise in the wind components than the ASCAT-coastal product, due to the smaller number of individual measurements contributing to the average radar cross section in a WVC. The ASCAT-6.25 product is intended for applications that demand a spatial resolution as high as possible, like the study of dynamical mesoscale phenomena.

**Index Terms**—Radar, wind.

## I. INTRODUCTION

SCATTEROMETER-DERIVED winds form a reliable and accurate source of wind information at the surface of the oceans. They are assimilated on a routine basis in numerical weather prediction (NWP) models and are used operationally in nowcasting applications like monitoring of tropical cyclones, e.g., [1]. They are also used for driving ocean models, and to investigate climate variability in both the atmosphere and the ocean, e.g., [2]. Process studies into dynamical mesoscale phenomena like coastal jets and convective storms require as high a spatial resolution as possible.

The advanced scatterometer (ASCAT) is one of the instruments carried by the Metop series of polar orbiting satellites operated by the European Organisation for the Exploitation of Meteorological Satellites (EUMETSAT). ASCAT-A was launched

in 2006, ASCAT-B in 2012, and the launch of ASCAT-C is scheduled for 2018. ASCAT operates at C-band (frequency 5.3 GHz) and uses six fan-beam antennas, three at each side of the satellite. Two beams look forward at  $45^\circ$  azimuth with respect to the satellite moving direction, two look cross-track at  $90^\circ$  azimuth, and two look backward at  $135^\circ$  azimuth [3].

The ASCAT wind data processor (AWDP) is the standard software for deriving ocean surface wind vectors from the radar measurements [4]. AWDP is developed in the framework of the EUMETSAT NWP Satellite Application Facility (NWPSAF) and may be obtained free of charge upon registration from the NWPSAF web pages ([www.nwpsaf.eu](http://www.nwpsaf.eu)). AWDP is used by the Ocean and Sea Ice Satellite Application Facility to produce global near real-time wind products ([www.osi-saf.org](http://www.osi-saf.org)) on grid sizes of 25 and 12.5 km.

The basic output of the ASCAT instrument consists of individual measurements by each of the three beams of the radar cross section,  $\sigma_0$ , as generated by the on-board processor. The spatial extent of an individual  $\sigma_0$  value is determined by beam width in azimuth and by on-board processing in range. It is described by its spatial response function (SRF). ASCAT wind processing uses cross sections averaged to a wind vector cell (WVC) grid. This averaging (or aggregation) is done separately for the fore, mid, and aft beams. Its purpose is to reduce the noise inherent in radar measurements and to ensure that all beams cover the same area as much as possible. The spatial extent of an aggregated cross section is given by its cumulative spatial response function (CSRF).

The ASCAT-25 wind product has a WVC grid size of 25 km, but the aggregated radar cross section for each beam (fore, mid, and aft) is obtained by averaging all individual  $\sigma_0$  values that fall in a 100 km by 100 km square box centered at the WVC under consideration. The average is spatially weighted with a Hamming window, so most of the radar cross section comes from a 50 km by 50 km area. The aggregated radar cross sections in the Hamming-filtered ASCAT-12.5 product are calculated in a similar way, except that the grid size is 12.5 km and the size of the averaging area (or aggregation area) is 50 km [5].

A disadvantage in these products is that the WVCs must be located quite far from the coast in order to avoid land contamination in the aggregation area. For ASCAT-12.5, the coast line separation is about 35 km, which is too large for many coastal applications. The ASCAT-coastal product also has a grid size of 12.5 km, but the aggregated radar cross section is the unweighted average of all individual  $\sigma_0$  values that fall in a circular box with 15 km radius centered at the WVC. This is the same approach as followed earlier for the QuikScat scatterometer carried by the SeaWinds satellite [6]. The 15 km value of the aggregation radius was determined by spectral comparison in open sea with the ASCAT-12.5 product [5]. For the open ocean, the two products have the same quality and therefore ASCAT-12.5 was

Manuscript received June 30, 2016; revised September 23, 2016; accepted October 23, 2016. This work was supported by EUMETSAT as part of the Satellite Application Facility for Numerical Weather Prediction (NWP SAF). (Corresponding author: Jur Vogelzang.)

J. Vogelzang, A. Stoffelen, A. Verhoef, and J. Verspeek are with the Royal Netherlands Meteorological Institute (KNMI), De Bilt, The Netherlands, GA 3731 (e-mail: Jur.Vogelzang@knmi.nl; Ad.Stoffelen@knmi.nl; Anton.Verhoef@knmi.nl; Jeroen.Verspeek@knmi.nl).

R. D. Lindsley was with the Microwave Earth Remote Sensing Laboratory, Brigham Young University, Provo, UT 84602 USA. He is now with the Remote Sensing Systems, Santa Rosa, CA 95401 USA (e-mail: lindsley@remss.com).

Color versions of one or more of the figures in this paper are available online at <http://ieeexplore.ieee.org>.

Digital Object Identifier 10.1109/JSTARS.2016.2623862

discontinued in April 2015. The smallest coastal distance in the ASCAT-coastal product is 20 km. Retrieving winds closer to the coast is currently not possible without accounting for the elongated shape of the SRFs (see Section III of this paper). EUMETSAT plans to implement a land fraction for each individual full-resolution measurement, which is computed from a land mask and the SRF [7].

In 2013, EUMETSAT started dissemination of a full-resolution radar cross-section product which contains the individual  $\sigma_0$  values generated by the on-board processor. It also contains a 6.25 km grid. This opened the possibility to define an operational ASCAT wind product on a 6.25 km grid processed in the same manner as the coastal product. The crucial parameter is the aggregation radius  $R$ : it must be smaller than 15 km (otherwise the true spatial resolution would not improve relative to ASCAT-coastal), but it must be large enough to capture enough individual  $\sigma_0$  values to ensure good radar cross-section statistics.

The approach in this study is less sophisticated than that outlined in [8], [9] and applied in [10], [11]. In those studies,  $\sigma_0$  is considered as a continuous field which is sampled by the scatterometer SRF. Deconvolution of the scatterometer measurements for each beam yields an estimate of the  $\sigma_0$  fields. These can be resampled on a fine grid. This approach allows for very high spatial resolutions, but its computational load makes it less attractive for operational use.

The aim of this paper is to characterize the true spatial resolution and accuracy of the new ASCAT-6.25 wind product as a function of  $R$  and to select the optimal choice for  $R$ . The true spatial resolution is estimated using the ASCAT SRF using the approach in [7]. The CSRf for each beam is obtained by summing the SRFs of all individual  $\sigma_0$  values within the aggregation area of a WVC, and normalizing the maximum value of the result to one. Similarly, the all-beam CSRf is obtained by summing the CSRfs of each of the three beams and again normalizing its maximum value to 1. The  $-3$  dB contour of the all-beam CSRf is a good indicator of the true spatial resolution. For ASCAT-coastal, the  $-3$  dB contour follows the edge of the aggregation area (the circular area with 15 km radius) quite well, leading to a true spatial resolution of about 28 km. For ASCAT-6.25, the CSRf is more elliptical, notably for the mid beam, due to the elongated SRF shape. The true spatial resolution varies with  $R$  and may range as low as 14 km for  $R = 5.0$  km, but the overlap between the beams is worse than for ASCAT-coastal and degrades with decreasing  $R$ . When beams do not overlap, they essentially observe slightly different parts of the ocean surface. As a result, wind variability will introduce variations in the average backscatter in each of the three beams, variations that are not consistent with the geophysical model function. This leads to so-called geophysical noise in the wind retrieval [12].

The ASCAT-6.25 product is shown to be noisier than ASCAT-coastal by using three methods: buoy comparison, triple collocation, and a novel method based on spatial variance analysis. The errors increase with decreasing  $R$ . All analyses give consistent results and indicate that a 7.5 km aggregation radius is a good compromise, giving an accuracy only slightly worse

than that of ASCAT-coastal and a spatial resolution of 17 km, which is clearly better than the 28 km found for ASCAT-coastal. To complete the quality assessment, the statistical consistency of ASCAT-6.25 with 7.5 km aggregation radius is shown to be slightly worse than that of ASCAT-coastal. This could be improved by better tuning of the error variances in the two-dimensional variational ambiguity removal scheme (2DVAR), both for ASCAT-6.25 and ASCAT-coastal, but that is considered outside the scope of this study.

The paper is organized as follows. The data used and some processing details are given in Section II. Section III deals with the spatial resolution based on the CSRf. Section IV contains the accuracy analysis of the ASCAT-6.25 winds retrieved for various values of the aggregation radius. A novel method for calculating the noise and its autocorrelation in the ASCAT-6.25 product relative to ASCAT-coastal is presented here, with some technical details in the Appendix. The comparison of statistical consistency is described in Section V. The results are discussed in Section VI, where it is argued that an aggregation radius of 7.5 km is a good compromise between spatial resolution and accuracy. Additionally, some suggestions for future improvement are presented here. The paper ends with conclusions in Section VII.

## II. DATA

In this study, we use all ASCAT-A data from August 2013. The data were processed on a 6.25 km grid with aggregation radii of 5, 7.5, 10, and 15 km. For the latter value, the product is identical with an oversampled ASCAT-coastal product. The ASCAT-6.25 product contains 162 WVCs per swath; 81 on each side of the satellite track. The KNMI quality flag, based on the inversion residual (MLE), was defined for the 7.5 km aggregation radius in the same manner as for the ASCAT-coastal and ASCAT-25 products. The inversion scheme of AWDP returns up to four solutions named ambiguities as well as the *a priori* probability of each ambiguity. As in the other AWDP products, the 2DVAR ambiguity removal scheme is used to select the most probable solution from these ambiguities.

During processing, the scatterometer winds are collocated with forecast winds from the ECMWF model as input for 2DVAR. The model winds, hereafter referred to as background, are interpolated quadratically in time and bilinearly in space to the scatterometer winds. The background winds are used as initial guess for the ambiguity removal, for monitoring purposes, and as data source in triple collocation. It must be stressed here that the background fields are not in the highest resolution available, but on a grid size of about 70 km, in order to guarantee continuity in operational 2DVAR processing. This grid size is sufficient for the purposes of this study.

Buoy data were obtained from the ECMWF MARS archive using all buoys not previously blacklisted. These buoy data are given as 10 min averages issued every hour, so the criteria for collocation with scatterometer data are a maximum temporal separation of 30 min and a maximum spatial separation of about 4.4 km (ASCAT-6.25 grid size divided by  $\sqrt{2}$ ). In cases where

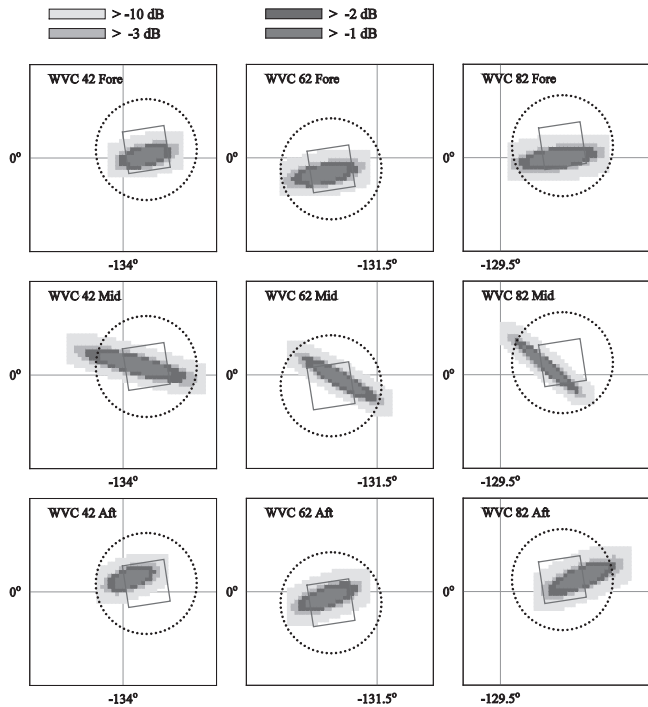


Fig. 1. Spatial response functions of a single ASCAT full-resolution radar cross-section measurement for the fore beam (top panels), mid beam (middle panels), and aft beam (bottom panels) for WVCs 42, 62, and 82 of the ASCAT-coastal product. The square box gives the WVC (size 12.5 km) and the dotted circle the boundary of the aggregation area (radius 15 km).

more collocations were found for the same buoy at the same time, the collocation closest in position was selected.

### III. SPATIAL RESOLUTION

The SRF for ASCAT, i.e., the spatial coverage of a single radar cross-section value in the full-resolution L1B EUMETSAT product, can be computed using the approach in [7]. As an illustration, Fig. 1 shows SRFs in dB of individual ASCAT radar cross sections, normalized to unit maximum value, with the colors indicating the value. SRFs are shown for the fore, mid, and aft beams (from top to bottom, respectively), and for WVC numbers 42, 62, and 82 (from left to right), corresponding respectively to lowest incidence angles, mid incidence angles, and highest incidence angles in the right-hand swath. The 12.5 km WVC is shown for reference, together with the boundary of the 15 km aggregation area. The WVCs lie on the right swath of an ascending orbit and are selected as close to the equator as possible in order to avoid distortion in the geographical grid.

Fig. 1 shows that the SRFs have an elliptical shape, caused by the antenna footprint, the range-gating, and the Doppler shift. The ellipses are quite elongated, notably for the mid beam. This is caused by on-board averaging of the antenna pulses: each full-resolution radar cross section is based on the running average of eight individual radar pulses. The chirps for the fore and aft beams go in different directions (low frequency to high frequency versus high to low), and Doppler shifts change the

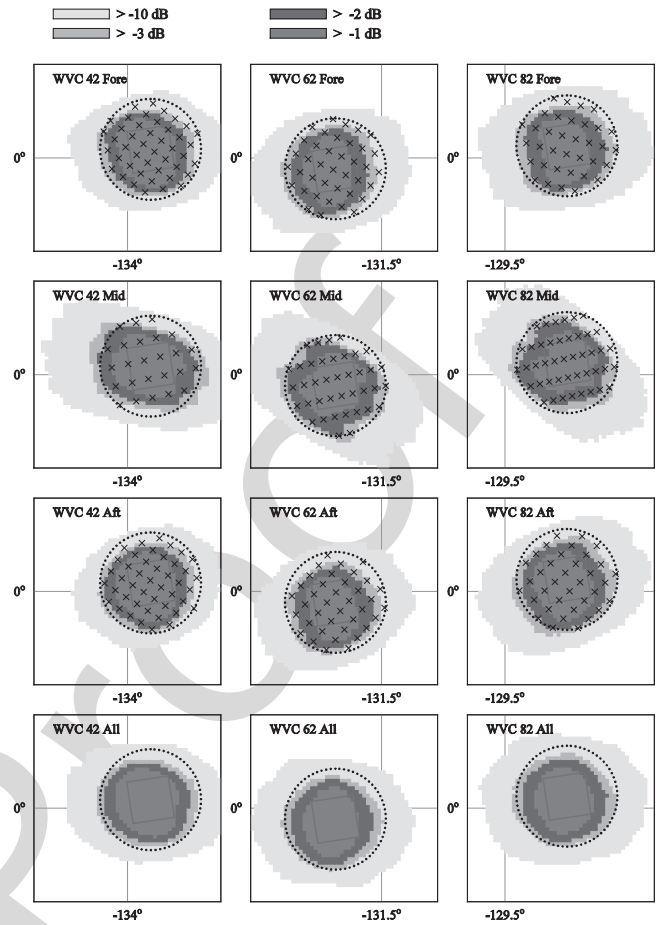


Fig. 2. Cumulative spatial response functions for ASCAT-coastal. The square box gives the WVC (size 12.5 km) and the dotted circle the boundary of the aggregation area (radius 15 km).

orientation of the ellipses in such a way that the fore and aft beam SRFs have almost the same orientation [7]. Fig. 1 also shows that the SRFs rapidly drop off to zero outside the  $-3$  dB contour.

For each beam separately, the CSRf for a WVC can be obtained by summing the SRFs contributing to that WVC and renormalizing to unit maximum value. The result for ASCAT-coastal is shown in Fig. 2. The colors indicate the CSRf value, the box represents the WVC boundary, the dotted circle the edge of the aggregation area, and the crosses the centers of the contributing SRFs. Note that the  $-3$  dB contour (CSRf equal to 0.501) follows the separation between orange and yellow, following quite well the edge of the circular aggregation area. The bottom row of panels in Fig. 2 shows the all-beam CSRf, i.e., the CSRf of all three beams combined, now without the centers of the contributing SRFs. The all-beam CSRf  $-3$  dB area also follows the edge of the aggregation area well, and its shape differs little from that of the CSRfs of the individual beams. This indicates good overlap between the three beams.

Fig. 3 shows the CSRf for ASCAT-6.25 with 7.5 km aggregation radius. As in Fig. 2, the WVC, the aggregation area boundary, and the contributing SRF centers are also shown, and

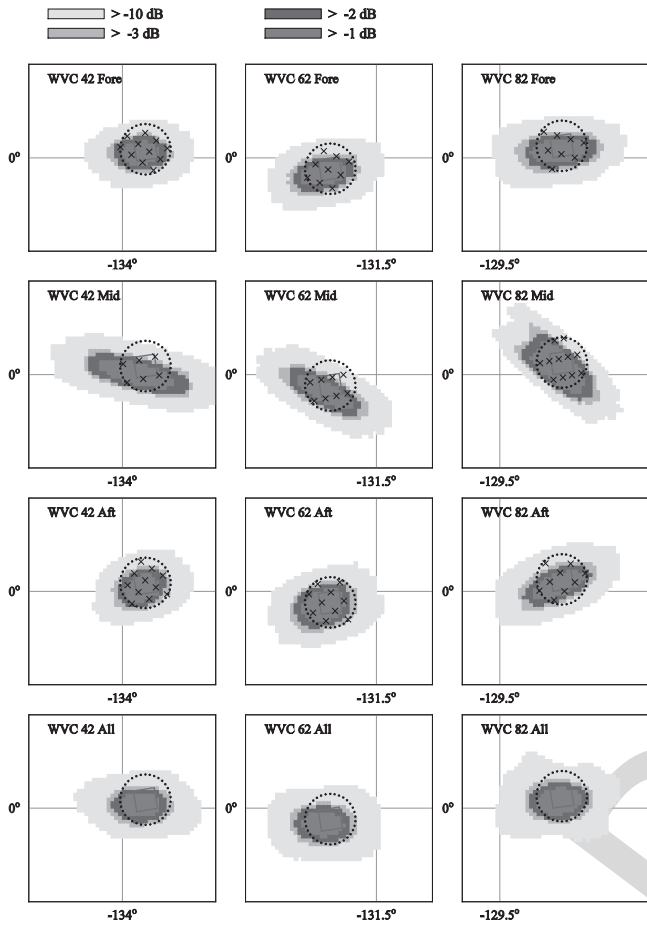


Fig. 3. Cumulative spatial response functions for ASCAT-6.25. The square box gives the WVC (size 6.25 km) and the dotted circle the boundary of the aggregation area (radius 7.5 km).

the bottom row of panels shows the CSRF of all three beams. In this case, the  $-3$  dB contour follows the aggregation area boundary less well, notably for the mid beam. The CSRFs have an elliptical shape, reflecting the shape of the contributing SRFs, notably for the mid beam at low incidence. A considerable portion of the CSRF may lie outside the aggregation area, and the difference in shape indicates poor overlap between the three beams. The CSRFs of all three beams (bottom row of panels in Fig. 3) are more circular, though for the three WVCs shown, it is located slightly southward of the aggregation area.

The true spatial resolution may be characterized by calculating the area of the CSRF enclosed by the  $-3$  dB contour. Fig. 4 shows that the area as a function of incidence angle for various values of the aggregation radius  $R$ . Fig. 4 shows results for the fore, mid, and aft beams separately, and for all beams together. The  $-3$  dB area varies slightly with the incidence angle, due to the varying shape and size of the SRFs over the swath. Note that the all-beam  $-3$  dB area (lower right panel of Fig. 4) is nearly constant with the incidence angle. Approximating the all-beam  $-3$  dB area by a circle and taking its diameter as a measure of the true spatial resolution (this is the full-width half-maximum measure), one arrives at 28 km for  $R = 15$  km (ASCAT-coastal), 20 km for  $R = 10$  km, 17 km for  $R = 7.5$  km, and 14 km for

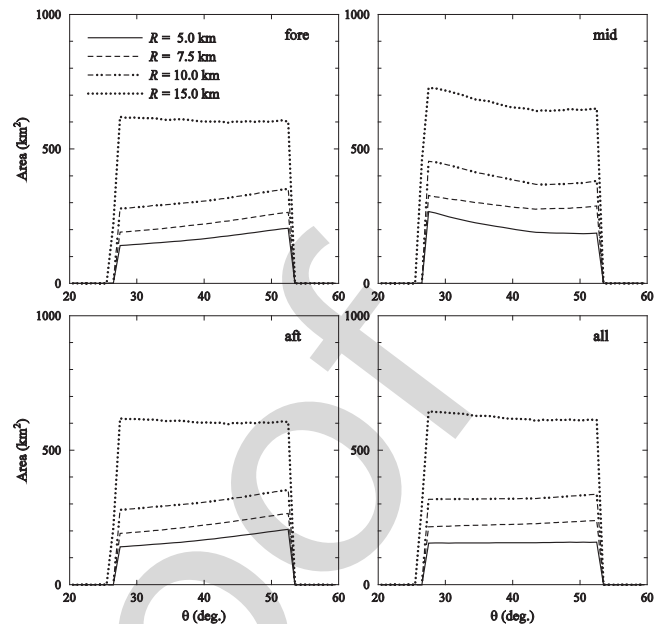


Fig. 4. Area within the  $-3$  dB CSRF contour versus incidence angle for ASCAT-6.25 at various aggregation radii for the fore, mid, and aft beams separately and for all beams together.

$R = 5$  km. Of course, the size of the SRFs poses a lower limit on the true spatial resolution defined this way.

Figs. 2 and 3 indicate that the overlap between the three beams gets worse as  $R$  decreases. Additionally, Fig. 4 gives some indication in that direction, as the area for all beams at  $R = 5.0$  km is smaller than the area of each individual beam. The overlap  $O_{\alpha\beta}$  between the CSRFs for beams  $\alpha$  and  $\beta$  can be quantified as

$$O_{\alpha\beta} = \frac{I_{\alpha\beta}^2}{I_{\alpha\alpha}I_{\beta\beta}} \quad (1)$$

with

$$I_{\alpha\beta} = \iint d\lambda d\phi \cos \phi C_{\alpha}(\lambda, \phi) C_{\beta}(\lambda, \phi) \quad (2)$$

where  $C_{\alpha}$  stands for the CSRF of beam  $\alpha$  as a function of geographical longitude  $\lambda$  and latitude  $\phi$ , and the integration is over the entire domain of the CSRFs. From (1) and (2), it is clear that the overlap  $O_{\alpha\beta}$  defined in this way equals one if the two CSRFs are identical and zero if they are disjoint.

Fig. 5 shows the overlap as a function of incidence angle for various aggregation radii. The overlap between the fore and the aft beam is very good and degrades only slightly with decreasing  $R$ . Figs. 2 and 3 show that this is due to the fact that the CSRF of each beam is elliptical, and that the ellipses have about the same orientation for the fore and aft beam. The CSRF ellipse of the mid beam makes an angle with that of the fore or aft beam, and indeed Fig. 5 shows poorer overlap between the mid and fore beams and between the mid and aft beams. As the CSRFs become more elliptical with decreasing  $R$ , the overlap of the fore or aft beam with the mid beam rapidly decreases with  $R$ . The  $-3$  dB CSRF areas

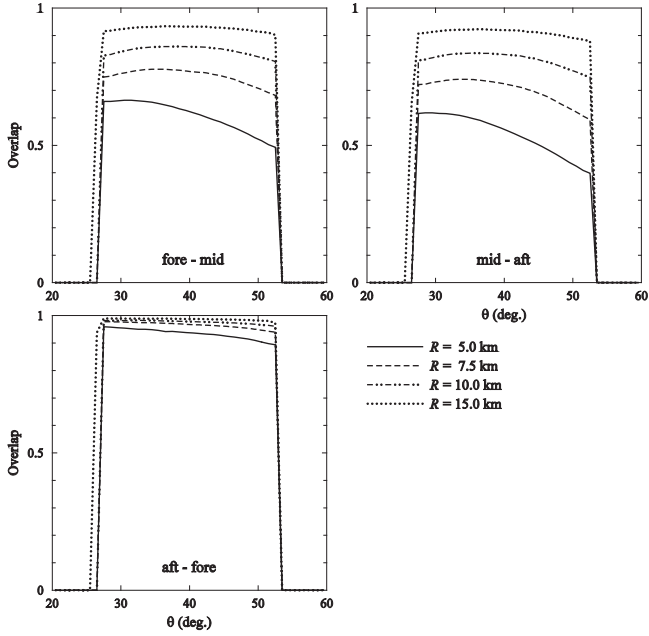


Fig. 5. Overlap between the three possible beam pairs versus incidence angle for ASCAT-6.25 at various aggregation radii.

TABLE I  
BUOY COMPARISON FOR AUGUST 2013

$R$ (km)	$\sigma_s$ (m/s)	$\sigma_d$ (deg)	$\sigma_l$ (m/s)	$\sigma_t$ (m/s)
5.0	1.01	17.9	1.70	1.42
7.5	0.99	16.6	1.64	1.39
10.0	0.98	16.9	1.61	1.37
15.0	0.98	16.8	1.59	1.36
Accuracy	0.02	0.3	0.03	0.03

and overlaps show no significant dependency on geographical latitude.

#### IV. ACCURACY

##### A. Buoy Comparison

Table I shows the standard deviations of the differences between scatterometer and buoy winds for wind speed, wind direction, wind component in the along-track direction  $l$ , and wind component in the cross-track direction  $t$ , for various values of the aggregation radius,  $R$ . The results in Table I are based on all available data from August 2013. Only collocations common to all values of  $R$  were taken into account, resulting in 2682 collocations. Wind direction statistics are based on a smaller number of collocations (between 1892 and 1907, depending on the value of  $R$ ), since these were only calculated for wind speeds exceeding 4 m/s. The accuracies in the last row of Table I are estimates based on the inverse square root of the number of collocations.

Table I shows that in general the differences between scatterometer and buoy winds tend to increase with decreasing

$R$ . However, the differences are hardly significant, except for  $R = 5$  km. Here, the differences are clearly larger, notably for the wind direction and the wind components.

##### B. Triple Collocation

Given three collocated datasets, triple collocation analysis allows to calculate the linear calibration coefficients of two sets relative to the third (reference) one and to retrieve the error in each dataset, provided that linear calibration is sufficient and that the errors are constant and independent [12], [13]. Table II shows the triple collocation results for August 2013 as a function of averaging radius  $R$ . It lists the error standard deviations for  $l$  and  $t$ ,  $\sigma_l$  and  $\sigma_t$ , the number of collocations used to arrive at the error estimates  $N$ , and the representativeness error variances obtained from the spatial variances at a scale of 200 km (see Section IV-C)  $r_l^2$  and  $r_t^2$ . The standard deviations of the errors in Table II are with respect to the scales resolved by the scatterometer, so the representativeness error is incorporated in the background error. The triple collocation analysis used only collocations that are common to all values of  $R$ . The last row gives the accuracy of the errors estimated under the assumption that the errors are Gaussian [13].

Table II shows that within the estimated accuracy, the buoy errors and the background errors do not depend on of the averaging radius, while the scatterometer errors increase with decreasing  $R$ , though the increase is only significant between  $R = 15$  km and  $R = 5$  km. The buoy errors are the same for  $l$  and  $t$ , whereas the scatterometer and background errors are larger for  $l$  than for  $t$ . The representativeness errors  $r_l^2$  and  $r_t^2$  increase with the decreasing value of  $R$ , indicating that indeed the scatterometer winds contain more detail than the ECMWF background winds. As stated at the beginning of this chapter, the background error estimates are for ECMWF forecasts on a 70 km grid.

##### C. Spatial Variance Error Model

The previous results suggest that decreasing the aggregation radius leads to higher spatial resolution, but also to more noise (larger errors) in the ASCAT-6.25 wind product. A common approach to such questions is spectral analysis. Fig. 6 shows the ASCAT-6.25 spectra for the wind components  $l$  (left-hand panel) and  $t$  (right-hand panel) for various values of the aggregation radius  $R$ . The spectra show a bump at high wavenumbers that increases as  $R$  decreases. This bump was previously observed in the spectra of the ASCAT-coastal product, but its exact origin was not clear. It is argued below that this is caused by correlated noise.

One problem in the interpretation of spectra like those in Fig. 6 is that they show the variance density in the wavenumber domain, but that this cannot be translated to the spatial domain in terms of spatial scales. Therefore, Vogelzang *et al.* [14] introduced a statistic called spatial variance. It is the cumulative variance as a function of scale (or sample length).

For a discrete equidistant dataset  $\{u_i\} = \{u(r_i)\}$  with  $r_i = i\Delta r$ ,  $i = 1, 2, \dots, N$ , the first and second moments for a sample

TABLE II  
TRIPLE COLLOCATION RESULTS FOR AUGUST 2013

$R$ (km)	Buoys		Scatterometer		Background		$N$	$r_l^2$ (m <sup>2</sup> /s <sup>2</sup> )	$r_t^2$ (m <sup>2</sup> /s <sup>2</sup> )
	$\sigma_l$ (m/s)	$\sigma_t$ (m/s)	$\sigma_l$ (m/s)	$\sigma_t$ (m/s)	$\sigma_l$ (m/s)	$\sigma_t$ (m/s)			
5.0	0.97	1.02	1.23	0.80	1.40	1.24	2655	1.10	1.37
7.5	1.00	1.02	1.11	0.74	1.39	1.22	2653	0.87	1.11
10.0	1.02	1.03	1.08	0.68	1.39	1.24	2655	0.75	0.97
15.0	1.01	1.04	1.02	0.65	1.40	1.21	2652	0.64	0.83
Accuracy	0.08	0.08	0.08	0.06	0.05	0.03			

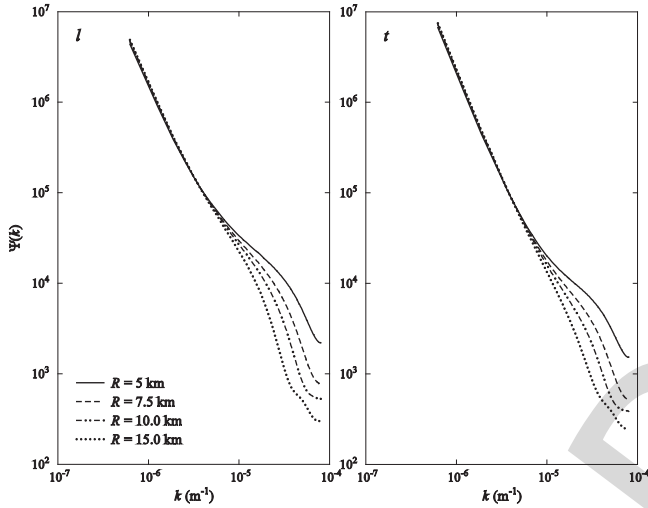


Fig. 6. ASCAT-6.25 spectra for the along-track and cross-track wind components at various aggregation radii.

of length  $n + 1$  (scale  $r_n = n\Delta r$  and lag  $n$ , where the lag is defined as the distance between two data points in units of the grid size) starting at a certain point  $u_i$  are defined as

$$M_1(i, n) = \frac{1}{n+1} \sum_{j=0}^n u_{i+j}, \quad M_2(i, n) = \frac{1}{n+1} \sum_{j=0}^n u_{i+j}^2. \quad (3)$$

The spatial variance is defined as the average variance of all samples with length  $n + 1$

$$V(n) = \langle M_2(i, n) - M_1^2(i, n) \rangle \quad (4)$$

where the brackets  $\langle \rangle$  denote averaging over all available samples, each sample being characterized by  $i$ , the index of its starting point. Its discrete derivative is defined as

$$\Delta V(n) = \frac{V(n) - V(n-1)}{\Delta r} \quad (5)$$

with  $V(0) = 0$ . The samples can be taken in the along-track direction, as in [14], but also in the cross-track direction, though the maximum lag size in that direction is limited by the swath width of 81 WVCs at each side of the satellite track for ASCAT-6.25.

Since the spatial variance  $V(n)$  is the cumulative variance contained in scales up to  $r_n$ , its derivative  $\Delta V(n)$  is the inc-

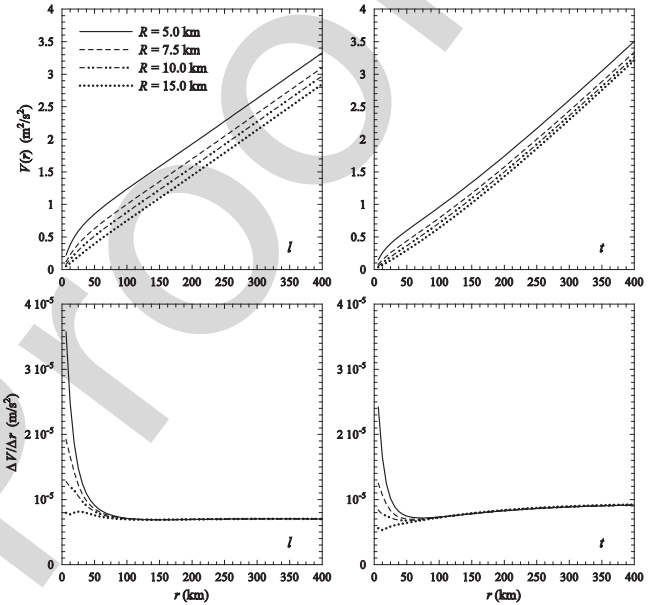


Fig. 7. ASCAT-6.25 spatial variance (top panels) and its derivative (bottom panels) for the wind components  $l$  (left-hand panels) and  $t$  (right-hand panels) at various aggregation radii.

rease in variance when going from scale  $r_{n-1}$  to  $r_n$  and can therefore be interpreted as a variance density. The difference between the spatial variances of scatterometer and background at a scale of 200 km is a good measure of the representativeness error. It has been used in the triple collocation analysis presented in Section IV-B.

Fig. 7 shows the along-track sampled spatial variances for the ASCAT-6.25 wind components  $l$  and  $t$  (top left and top right panels, respectively) as well as their discrete derivative (bottom left and bottom right panels). Fig. 7 shows that  $V$  increases rapidly for scales below 100 km, notably for small values of  $R$ . This behavior is seen more clearly in the plots of  $\Delta V$ : at small lags, a peak is visible that gets higher as  $R$  gets smaller. For  $R = 15$  km (oversampled ASCAT-coastal), the peak has almost disappeared. The peak has its maximum at the first lag, so increase in noise with decreasing  $R$  seems a plausible explanation for it. Since the aggregation areas of neighboring WVCs overlap, also at  $R = 5$  km, the noise must be correlated.

TABLE III  
SPATIAL VARIANCE ERROR ANALYSIS RESULTS FOR THE ALONG-TRACK  
SAMPLED  $l$  COMPONENT OF ASCAT-6.25 WITH  $R = 5$  km AS A FUNCTION  
OF  $J$

$J$	$\sigma^2$	$\rho_1$	$\rho_2$	$\rho_3$	$\rho_4$	$\rho_5$	$\rho_6$
1	0.347	0	0	0	0	0	0
2	0.571	0.392	0	0	0	0	0
3	0.598	0.420	0.045	0	0	0	0
4	0.571	0.393	0.000	-0.047	0	0	0
5	0.547	0.367	-0.044	-0.093	-0.044	0	0
6	0.532	0.348	-0.073	-0.124	-0.074	-0.028	0
7	0.522	0.335	-0.095	-0.147	-0.095	-0.049	-0.020

TABLE IV  
SPATIAL VARIANCE ERROR ANALYSIS RESULTS FOR AUGUST 2013

Sampling type	$R$ (km)	$l$			$t$		
		$\sigma^2$ ( $\text{m}^2/\text{s}^2$ )	$\rho_1$	$\rho_2$	$\sigma^2$ ( $\text{m}^2/\text{s}^2$ )	$\rho_1$	$\rho_2$
Along track	5.0	0.60	0.42	0.05	0.39	0.40	0.04
	7.5	0.33	0.57	0.13	0.20	0.56	0.11
	10.0	0.17	0.66	0.23	0.10	0.65	0.23
Cross track	5.0	0.51	0.23	0.01	0.38	0.25	0.01
	7.5	0.26	0.47	0.06	0.19	0.49	0.07
	10.0	0.14	0.60	0.23	0.10	0.62	0.24

The spatial variance is a linear combination of the second-order structure function at various distances, which in turn is the Fourier transform of the spectrum [14], see also the Appendix. Therefore, the change in the spectral shape with  $R$  in Fig. 6 is attributed to correlated noise. Note that uncorrelated (white) noise would lead to a constant noise floor.

This interpretation of Figs. 6 and 7 is supported by experiments with simulated data, a few examples of which are presented in the Appendix. There it is also shown that if the noise contribution can be isolated, so  $\Delta V = \Delta V^{(S)} + \Delta V^{(N)}$ , it is possible to calculate the noise variance and its correlation coefficients. The bottom panels of Fig. 7 suggest to take  $\Delta V$  for  $R = 15$  km as  $\Delta V^{(S)}$ , since here almost no noise peak is visible. Application of the spatial variance error model from the Appendix thus yields results with respect to the ASCAT-coastal product. The number of correlation coefficients involved must be determined *a posteriori* as follows. As an example, Table III gives the results for the along-track sampled wind component  $l$  of ASCAT-6.25 with  $R = 5$  km as a function of  $J$  the number of lags taken into account. For  $J = 1$ , only the variance  $\sigma^2$  can be retrieved; for  $J > 1$ , also  $J - 1$  correlations can be found. The highest variance,  $\sigma^2 = 0.598 \text{ m}^2/\text{s}^2$  is found for  $J = 3$ . Here, positive correlations are found at lags 1 and 2 (neighbors and next-neighbors). For higher values of  $J$ , the additional correlation coefficients become small and negative, indicating that the  $J = 3$  results are the most reliable. Moreover, from geometrical considerations, one does not expect correlations from lag 3 or higher.

Table IV shows the results for the excess variance and its correlations with respect to  $R = 15$  km as a function of  $R$

TABLE V  
EXCESS VARIANCES W.R.T. 15 KM AVERAGING RADIUS FROM TRIPLE  
COLLOCATION (TC) AND SPATIAL VARIANCE ANALYSIS (SV)

$R$ (km)	$\Delta\sigma_l^2$ ( $\text{m}^2/\text{s}^2$ )		$\Delta\sigma_t^2$ ( $\text{m}^2/\text{s}^2$ )	
	TC	SV	TC	SV
5.0	0.52	0.60	0.25	0.39
7.5	0.21	0.33	0.14	0.30
10.0	0.10	0.17	0.06	0.10

for the wind components  $l$  and  $t$ . The excess variance increases with decreasing  $R$  for both  $l$  and  $t$ , and for both along-track and cross-track sampling, while the correlation coefficients decrease. This is consistent with the notion that smaller aggregation areas lead to noisier radar cross sections and also to less overlap between the CSRFs of the beams (see Fig. 5). For the along-track wind component  $l$ , the error model yields slightly higher excess noise variances with along-track sampled spatial variances than with cross-track sampled ones, while for the cross-track wind component  $t$  both sampling types give very similar results. The correlation coefficients show a clear dependency on the sampling type, caused by different overlaps of the CSRFs (see Figs. 1 and 3). They are remarkably similar for  $l$  and  $t$ .

#### D. Comparison

The spatial variance error analysis shows a considerable increase in noise w.r.t. the ASCAT coastal product when going to a smaller averaging radius. This is confirmed by the buoy comparison and the triple collocation analysis, but only significantly between  $R = 15$  km and  $R = 5$  km.

The accuracy of the spatial variance error model results is hard to estimate. It depends not only on the statistical accuracy of the spatial variances themselves, but also on the relation between spatial variances and second-order structure functions, which becomes approximate when the dataset contains missing points and the sampling strategy may become important. However, sampling effects on the error model are expected to be small, because the noise contribution is obtained by subtracting a reference spatial variance that has been sampled in the same way. An error of about  $0.05 \text{ m}^2/\text{s}^2$  in the error variance therefore seems reasonable. It leads to consistent results in Table IV and is in agreement with the accuracies estimated from triple collocation. The spatial variance analysis assumes that the signal content of the various wind products is independent of the averaging radius. When going to smaller averaging radius, one expects the effective resolution to improve and thus the signal content at small distances to increase. Therefore, the spatial variance analysis may overestimate the errors because its reference level is too low.

Table V gives the excess variances calculated from the triple collocation results (by taking the values for  $R = 15$  km from Table III as reference, labeled TC) and from the spatial variance analysis (from Table IV, labeled SV). The spatial variance

analysis indeed yields slightly higher values for the excess variance than the triple collocation analysis, but the difference is small and hardly significant because of the limited accuracy of the triple collocation results. Moreover, the spatial variance analysis covers all Earth, while the triple collocation analysis is restricted to the buoy locations. Nevertheless, these results indicate that both methods give consistent results.

## V. STATISTICAL CONSISTENCY

The normalized inversion residual, MLE, can be converted to an *a priori* probability  $p$ , that an ambiguous solution returned by the inversion algorithm is the correct solution. This can be verified after ambiguity removal by calculating  $P(\text{sel}|p)$ , the probability that a solution is selected given its *a priori* probability. Fig. 8 shows the probability density function (pdf) of  $P(\text{sel}|p)$  against  $p$  for ASCAT-6.25 with 7.5 km aggregation radius (solid curve) and for ASCAT-coastal (dashed curve). In case of perfect statistical consistency, the pdf of  $P(\text{sel}|p)$  would increase linearly from value zero at  $p = 0$  to value two at  $p = 1$  (so that the integrated pdf equals one), as indicated by the dotted line in Fig. 8.

The overall statistical consistency is quite good, but  $P(\text{sel}|p)$  is slightly too high for low values of  $p$  and slightly too low for high values of  $p$ . This deviation from perfect statistical consistency is stronger for ASCAT-6.25 than for ASCAT-coastal. This means that the 2DVAR ambiguity removal scheme selects too many ambiguities with low *a priori* probability and too few with high probability. Apparently, 2DVAR puts too much weight on spatial consistency at the cost of statistical consistency. This might be improved by tuning the 2DVAR parameters, but that is outside the scope of this study.

## VI. DISCUSSION

The results in Section III show that the  $-3$  dB area of the all-beam CSRF varies with aggregation radius  $R$  from more than  $600 \text{ km}^2$  for  $R = 15 \text{ km}$  (ASCAT-coastal) to about  $150 \text{ km}^2$  for  $R = 5 \text{ km}$ . Assuming a circular shape for the CSRF, the true spatial resolution is defined as the diameter of this circle. It is about  $28 \text{ km}$  for ASCAT-coastal and about  $20 \text{ km}$  for  $R = 10 \text{ km}$ ,  $17 \text{ km}$  for  $R = 7.5 \text{ km}$ , and  $14 \text{ km}$  for  $R = 5 \text{ km}$ . Though the ASCAT-6.25 CSRF for  $R = 7.5 \text{ km}$  is elliptical in shape rather than circular, Fig. 3 shows that a true spatial resolution of about  $17 \text{ km}$  is indeed a good estimate.

The results in Section IV show that ASCAT-6.25 wind products with an averaging radius smaller than  $15 \text{ km}$  contain more noise than ASCAT-coastal, as identified by buoy comparison, triple collocation, and spatial variance analysis. The noise increases rapidly with decreasing  $R$ .

An aggregation radius of  $7.5 \text{ km}$ , half of that for the ASCAT-coastal product, is a good compromise between wind quality and spatial resolution: it yields a true spatial resolution of about  $17 \text{ km}$ , clearly better than the  $28 \text{ km}$  for ASCAT-coastal, while the excess noise variance (relative to ASCAT coastal) is only  $0.2 \text{ m}^2/\text{s}^2$ . This value is therefore adopted as default in AWDP, though it is under user control with a command line argument.

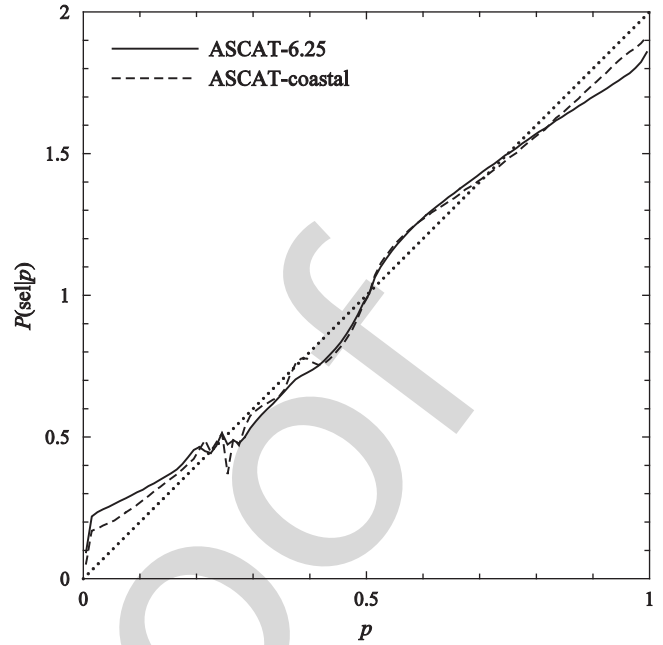


Fig. 8. Statistical consistency for ASCAT-6.25 at 7.5 km aggregation radius and ASCAT-coastal.

Fig. 3 also shows that for the default ASCAT-6.25 the contributing SRFs may not be divided evenly over the aggregation area, causing the CSRF to be shifted with respect to the WVC centre. This adds to the poor overlap between the CSRFs of the three beams, see Fig. 5, which, in turn, leads to geophysical errors because different beams sample different parts of the ocean surface. This is in particular unwanted in dynamic areas—just the type of situation where high-resolution wind fields are of interest. Such detrimental effects can be mitigated by optimizing the SRF sampling using a WVC grid synchronized to the mid-beam antenna pattern. This approach is beyond the scope of this paper, but is discussed further in [15]. The statistical consistency of ASCAT-6.25 with 7.5 km aggregation radius is slightly worse than that of ASCAT-coastal. In principle, this could be improved by better tuning of the error variances in 2DVAR, but that is also considered outside the scope of this paper. Moreover, the degradation in statistical consistency is at an acceptable level and must be balanced against a better true spatial resolution.

Despite its nonoptimal SRF sampling, ASCAT-6.25 clearly has added value compared to ASCAT-coastal: it is capable of detecting smaller features as the cost of slightly more noise. As an example, Fig. 9 shows von Kármán vortices in the wake of Madeira recorded August 4, 2013, for ASCAT-coastal (top panel) and ASCAT-6.25 (bottom panel). Though the vortices are recognizable in ASCAT-coastal, they show more detail in ASCAT-6.25.

At this moment, the OSI SAF has no plans to disseminate a near real-time ASCAT-6.25 product, so interested users have to do their own processing. This may be reconsidered in case of sufficient user demand.

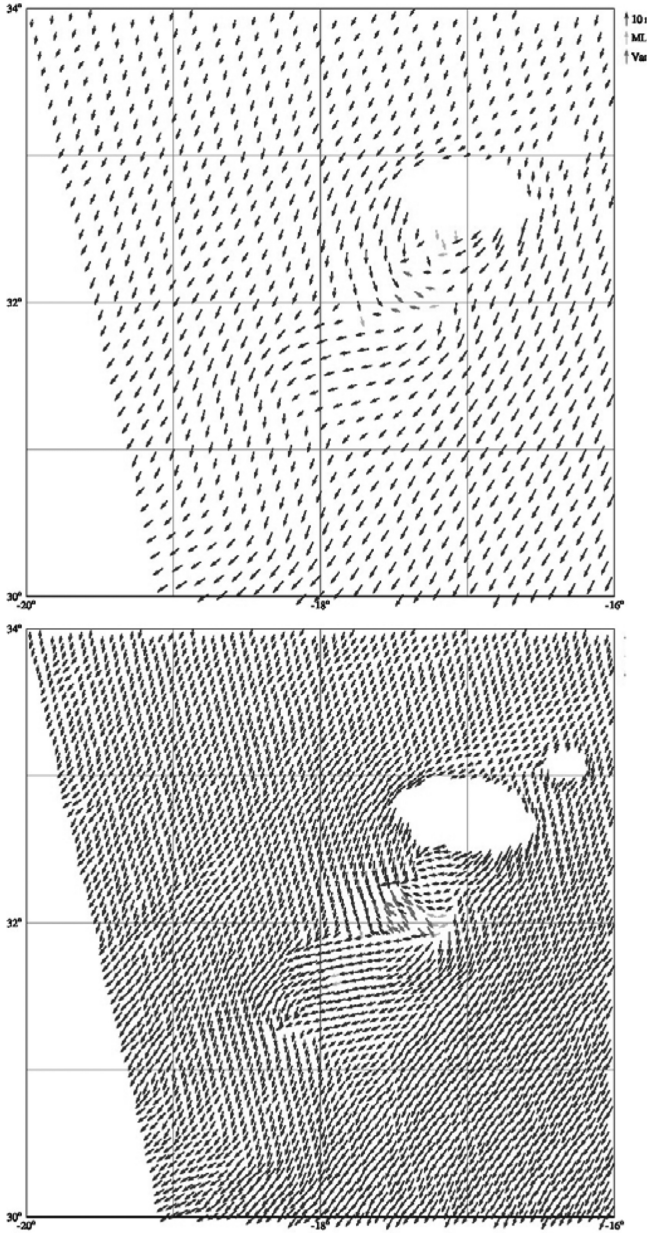


Fig. 9. ASCAT-coastal (top panel) and ASCAT-6.25 (bottom panel) wind field on August 4, 2013 at about 22:00 showing von Kármán vortices southwest of the isle of Madeira. The isle reveals itself as the area of missing wind vectors south of 33 °N, -17 °E).

## VII. CONCLUSION

From version 2.4 onward, the AWDP is able to process full-resolution L1B radar cross-section data to a wind product on a 6.25 km grid. The aggregation radius  $R$  is the crucial parameter. A value of 7.5 km, half of that for ASCAT-coastal, yields the best compromise between spatial resolution and wind accuracy and is chosen as default value in AWDP. Taking the -3 dB contour of the CSRF as a measure for the true spatial resolution, the ASCAT-6.25 resolution is about 17 km, better than the 28 km of ASCAT-coastal. Buoy comparison, triple collocation, and spatial variance analysis show that the default ASCAT-6.25 product also contains slightly more noise ( $0.2 \text{ m}^2/\text{s}^2$  more vari-

ance in the wind components) than the ASCAT-coastal product. This is due to the fact that less SRFs contribute to the CSRF, notably for the mid beam at small incidence angles. This leads to more noise in the average radar cross sections and, hence, in the retrieved winds. Also the overlap between the CSRFs of the three beams is poorer for ASCAT-6.25 than for ASCAT-coastal, leading to larger geophysical noise. Nevertheless, the ASCAT-6.25 wind product is valuable in studying dynamical mesoscale features like convection cells, coastal jets, and von Kármán vortices.

## APPENDIX SPATIAL VARIANCE ERROR ANALYSIS

Suppose we have a dataset  $\{u_i\} = \{u(r_i)\}$  with  $r_i = i\Delta r$ ,  $i = 0, 1, \dots, n$ . Suppose further that the data contain noise, so that  $u_i = s_i + \varepsilon_i$  with  $s_i$  the pure signal and  $\varepsilon_i$  the noise. The increment at lag  $j$ ,  $\delta_{i,j} = u_i - u_{i+j}$ , can be split into a signal part and a noise part as

$$\delta_{i,j} = (s_i - s_{i+j}) + (\varepsilon_i - \varepsilon_{i+j}). \quad (\text{A.1})$$

The second-order structure function at lag  $j$  is defined as

$$D_j = \langle \delta_{i,j}^2 \rangle \quad (\text{A.2})$$

where the brackets  $\langle \rangle$  denote averaging over all samples in the dataset. Assuming that the noise is not correlated with the signal strength, so  $\langle (s_i - s_{i+j})(\varepsilon_i - \varepsilon_{i+j}) \rangle = 0$ , the structure function can also be written as the sum of a signal part  $D_j^{(S)}$  and a noise part,  $D_j^{(N)}$ , with

$$D_j^{(S)} = \langle (s_i - s_{i+j})^2 \rangle, \quad (\text{A.3})$$

$$D_j^{(N)} = \langle (\varepsilon_i - \varepsilon_{i+j})^2 \rangle = 2\sigma^2(1 - \rho_j) \quad (\text{A.4})$$

where  $\sigma^2 = \langle \varepsilon_i^2 \rangle = \langle \varepsilon_{i+j}^2 \rangle$  is the noise variance and  $\rho_j = \langle \varepsilon_i \varepsilon_{i+j} \rangle$  the noise autocorrelation. The spatial variance  $V_j$  is defined in [9]. It is related to the second-order structure function by the Yates relation [16]

$$V_j = \frac{1}{(j+1)^2} \sum_{k=1}^j (j+1-k) D_k. \quad (\text{A.5})$$

Since the relation between spatial variance and second-order structure function is linear, also the spatial variance can be split in a signal part and a noise part,  $V_j = V_j^{(S)} + V_j^{(N)}$ , with

$$V_j^{(S)} = \frac{1}{(j+1)^2} \sum_{k=1}^j (j+1-k) D_k^{(S)}, \quad (\text{A.6})$$

$$V_j^{(N)} = \frac{2\sigma^2}{(j+1)^2} \sum_{k=1}^j (j+1-k) (1 - \rho_k). \quad (\text{A.7})$$

The effect of noise is most clearly exhibited by the discrete derivative of the spatial variance,

$$\Delta V_j = \frac{V_j - V_{j-1}}{\Delta r} \quad (\text{A.8})$$

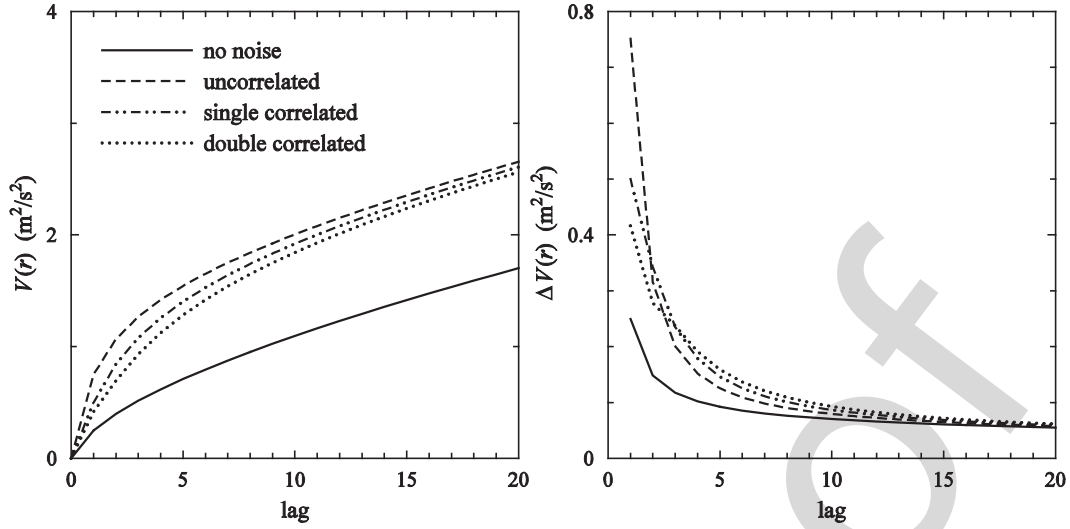


Fig. A1. Spatial variance (left-hand panel) and its derivative (right-hand panel) as a function of lag size for a fractional Brownian motion process with exponent  $2/3$  without noise (solid curves), uncorrelated noise (dashed curves), single correlated noise (dotted–dotted–dashed curves) and double correlated noise (dotted curves).

TABLE A1  
ERROR ANALYSIS RESULTS FOR FRACTIONAL BROWNIAN MOTION WITH  
CORRELATED GAUSSIAN NOISE

J	$\sigma^2$	$\rho_1$	$\rho_2$	$\rho_3$	$\rho_4$	$\rho_5$
1	0.199	0	0	0	0	0
2	0.398	0.498	0	0	0	0
3	0.596	0.665	0.333	0	0	0
4	0.795	0.749	0.500	0.250	0	0
5	0.995	0.800	0.600	0.401	0.201	0
6	0.995	0.800	0.600	0.401	0.201	0.00005
Exact	1.0	0.8	0.6	0.4	0.2	0.0

with  $j > 0$  and  $V_0 = 0$ .  $\Delta V_j$  is the increase in variance when going from scale  $r_{j-1}$  to  $r_j$ . From the foregoing, it is clear that it too can be split in a signal part and a noise part. From (A.7) and (A.8), one obtains for the noise part

$$\Delta V_j^{(N)} = \frac{\sigma^2}{\Delta r} \sum_{k=1}^j 2^k \frac{(2j+1) - j(j-1)}{j^2(j+1)^2} (1 - \rho_k). \quad (\text{A.9})$$

If the noise is uncorrelated, i.e.,  $\rho_k = 0$  for all  $k$ , (A.9) reduces to

$$\Delta V_j^{(N)} = \frac{\sigma^2}{\Delta r} \frac{1}{j(j+1)}. \quad (\text{A.10})$$

In this case,  $\Delta V_j^{(N)}$  peaks at lag 1 and the peak height drops quadratically with the lag number. For correlated noise, the peak may become lower and shifted to higher lag numbers, depending on the nature of the correlations.

As an example, Fig. A1 shows  $V_j$  and  $\Delta V_j$  against lag number  $j$  for a fractional Brownian motion (FBM) process with exponent  $2/3$  and unit grid size. The solid curve is without noise. Its second-order structure function has a  $2/3$  power law behavior, and so has its spatial variance [13]. The derivative of the spatial variance, therefore, follows a power law with exponent  $-1/3$  which causes in this case a peak at low lag numbers. The dashed curves are with uncorrelated Gaussian noise of unit variance.

Now the noise peak at low lag numbers is clearly visible. When the noise is correlated with neighbors (dotted–dotted–dashed curves) and next-neighbors (dotted curves) the noise peak get lower and broader.

Equation (A.9) can be written in compact form as

$$\Delta V_j^{(N)} = \frac{\sigma^2}{\Delta r} \sum_{k=1}^j C_{jk} R_k \quad (\text{A.11})$$

with  $R_k = 1 - \rho_k$  and

$$C_{jk} = \begin{cases} 2^k \frac{(2j+1) - j(j-1)}{j^2(j+1)^2}, & k \leq j \\ 0, & k > j \end{cases}. \quad (\text{A.12})$$

Suppose we have values of  $\Delta V_j^{(N)}$  for  $j = 1, 2, \dots, J$ . Equation (A.11) defines a system of  $J$  equations with  $J+1$  unknowns  $R_j$ ,  $j = 1, 2, \dots, J$  and  $\sigma^2$ . This system can be solved under the assumption that the correlation coefficient becomes zero for lag  $J$ , so  $R_J = 1 - \rho_J = 1$ . This assumption can be tested afterward by varying  $J$ .

To cast (A.11) in a form more suitable for solution, first divide all equations by  $\Delta V_1^{(N)}$  to eliminate  $\sigma^2$  and  $\Delta r$

$$\frac{\Delta V_j^{(N)}}{\Delta V_1^{(N)}} = \sum_{k=1}^j C_{jk} \frac{R_k}{C_{11} R_1}, \quad j = 2, 3, \dots, J. \quad (\text{A.13})$$

Multiplying with  $C_{11} R_1$ , rearranging terms, and introducing  $\Delta_j = \Delta V_j^{(N)} / \Delta V_1^{(N)}$  yields

$$-C_{11} \Delta_j R_1 + \sum_{k=1}^j C_{jk} R_k = 0, \quad j = 2, 3, \dots, J. \quad (\text{A.14})$$

Since  $R_J = 1$  this is a system of  $J-1$  equations with  $J-1$  unknowns. This system is easily triangularized and solved. The variance can then be retrieved from (A.11) for  $j = 1$  as

$$\sigma^2 = \frac{\Delta r \Delta V_1^{(N)}}{C_{11} R_1}. \quad (\text{A.15})$$

The procedure outlined above has been tested on a dataset containing  $2^{20}$  values from a FBM process with exponent  $2/3$ . Gaussian noise of unit variance was added to it, and the noise was made correlated using a running average so that  $\rho_1$  to  $\rho_4$  have values 0.8, 0.6, 0.4, and 0.2, respectively. The results for  $J$  running from 1 to 6 are shown in Table A1. The table shows that the variance and the correlation coefficients converge to their exact values shown in the bottom row as  $J$  increases to 5. The value of  $\sigma^2$  is retrieved with an accuracy of about 0.005, those of the correlation coefficients with an accuracy of about 0.001. This is of the order of the inverse square root of the number of points in the dataset. For  $J = 6$ , the excess correlation coefficient  $\rho_5$  is smaller than the accuracy, consistent with zero value. This holds also for higher correlation coefficients at higher values for  $J$ . Note that the variance is underestimated when an insufficient number of correlation coefficients is assumed ( $J < 5$ ).

#### ACKNOWLEDGMENT

The Fractional Brownian Motion data were kindly provided by G. P. King (ICM, Barcelona, Spain) using the free MATLAB code developed by A. Holtsberg. The authors wish to thank J. Bidlot (ECMWF) for his assistance in obtaining buoy measurements.

#### REFERENCES

- [1] J. Sienkiewicz *et al.*, "Impact of the loss of QuikSCAT on NOAA MWS marine warning and forecast operations," presented at the First International Ocean Vector Winds Science Team Meeting, Barcelona, Spain, May 2010. [Online]. Available: [http://coaps.fsu.edu/scatterometry/meeting/past.php#2010\\_may](http://coaps.fsu.edu/scatterometry/meeting/past.php#2010_may)
- [2] M. Bourassa *et al.*, "Remotely sensed winds and wind stresses for marine forecasting and ocean modeling," in *Proc. OceanObs09 Sustained Ocean Observ. Inf. Soc.*, 2010, vol. 2, doi:10.5270/OceanObs09.cwp.08.
- [3] J. Figa-Saldaña, J. Wilson, E. Attema, R. Gelsthorpe, M. Drinkwater, and A. Stoffelen, "The advanced scatterometer (ASCAT) on the meteorological operational (MetOp) platform: A follow on for the European wind scatterometers," *Can. J. Remote Sens.*, vol. 28, pp. 404–412, 2002, doi:10.5589/m02-035.
- [4] *ASCAT Wind Product User Manual*, KNMI, De Bilt, The Netherlands, 2013. [Online]. Available: [http://projects.knmi.nl/scatterometer/publications/pdf/ASCAT\\_Product\\_Manual.pdf](http://projects.knmi.nl/scatterometer/publications/pdf/ASCAT_Product_Manual.pdf)
- [5] A. Verhoef, M. Portabella, and A. Stoffelen, "High resolution ASCAT scatterometer winds near the coast," *IEEE Trans Geosci. Remote Sens.*, vol. 50, no. 7, pp. 2481–2487, Jul. 2012, doi:10.1109/TGRS.2011.2175001.
- [6] R. S. Dunbar *et al.*, *QuikSCAT Science Data Product User Manual, Version 3.0, JPL Document D-18053—Rev A*, Jet Propulsion Laboratory, Pasadena, CA, USA, Sep. 2006.
- [7] R. D. Lindsley, C. Anderson, J. Figa-Saldaña, and D. Long, "A parameterized ASCAT measurement spatial response function," *IEEE Trans. Geosci. Remote Sens.*, vol. 54, no. 8, pp. 4570–4579, Aug. 2016, doi:10.1109/TGRS.2016.2544835.
- [8] D. S. Early and D. G. Long, "Image reconstruction and enhanced resolution imaging from irregular samples," *IEEE Trans. Geosci. Remote Sens.*, vol. 39, no. 2, pp. 291–302, Feb. 2001, doi:10.1109/36.905237.
- [9] D. G. Long, P. Hardin, and P. Whiting, "Resolution enhancement of spaceborne scatterometer data," *IEEE Trans. Geosci. Remote Sens.*, vol. 31, no. 3, pp. 700–715, May 1993, doi:10.1109/36.225536.
- [10] R. Lindsley and D. G. Long, "Enhanced-resolution reconstruction of ASCAT backscatter measurements," *IEEE Trans. Geosci. Remote Sens.*, vol. 54, no. 5, pp. 2589–2601, May 2016, doi:10.1109/TGRS.2015.2503762.
- [11] R. D. Lindsley, J. R. Blodgett and D. G. Long, "Analysis and validation of high-resolution wind From ASCAT," *IEEE Trans. Geosci. Remote Sens.*, vol. 54, no. 10, pp. 5699–5711, Oct. 2016, doi:10.1109/TGRS.2016.2570245.
- [12] A. Stoffelen, "Toward the true near-surface wind speed: error modeling and calibration using triple collocation," *J. Geophys. Res.*, vol. 103, pp. 7755–7766, 1998.
- [13] J. Vogelzang, A. Stoffelen, A. Verhoef, and J. Figa-Saldaña, "On the quality of high-resolution scatterometer winds," *J. Geophys. Res.*, vol. 116, 2011, Art. no. C10033, doi:10.1029/2010JC006640.
- [14] J. Vogelzang, G. P. King, and A. Stoffelen, "Spatial variances of wind fields and their relation to second-order structure functions and spectra," *J. Geophys. Res. Oceans*, vol. 120, pp. 1048–1064, 2015, doi:10.1002/2014JC010239.
- [15] J. Vogelzang and A. Stoffelen, "ASCAT ultra high resolution wind products on optimised grids," *J. Sel. Topics Remote Sens.*, 2016, doi:10.1109/JSTARS.2016.2623861.
- [16] F. Yates, "Systematic sampling," *Philosoph. Trans. Roy. Soc.*, vol. A241, pp. 345–377, 1948, doi:10.1098/rsta.1948.0023.



**Jur Vogelzang** was born in 1955, in The Netherlands. He received the M.Sc. degree in theoretical physics from the Free University, Amsterdam, The Netherlands, in 1981, and the Ph.D. degree in physics on radar remote sensing from the University of Utrecht, Utrecht, The Netherlands, in 1998.

He is currently with the Royal Netherlands Meteorological Institute (KNMI), De Bilt, The Netherlands, where he is working on scatterometer wind products.



**Ad Stoffelen** was born in 1962, in The Netherlands. He received the M.Sc. degree in physics from the Technical University of Eindhoven, Eindhoven, The Netherlands, in 1987, and the Ph.D. degree in meteorology on scatterometry from the University of Utrecht, Utrecht, The Netherlands.

He currently leads a group on active satellite sensing at KNMI and is involved in topics from future missions and retrieval to 24/7 operations, user training and services. He is also deeply involved in the European Space Agency ADM-Aeolus Doppler Wind

Lidar mission.



**Richard D. Lindsley** (S'08–M'16) received the Ph.D. degree in electrical engineering from Brigham Young University (BYU), Provo, UT, USA, in 2015.

From 2008 to 2015, he was with the Microwave Earth Remote Sensing Laboratory, BYU. He is currently with the Remote Sensing Systems, Santa Rosa, CA, USA. His research interests include microwave remote sensing and signal processing.



**Anton Verhoef** was born in 1964, in The Netherlands. He received the M.Sc. degree in physics and the Ph.D. degree in solid state physics from the Rijksuniversiteit Groningen, Groningen, The Netherlands, in 1989 and 1994, respectively.

He is currently with the Royal Netherlands Meteorological Institute (KNMI), De Bilt, The Netherlands, and is working on scatterometry processing software development, data validation, quality monitoring, and user services.



**Jeroen Verspeek** was born in 1962, in The Netherlands. He received the M.Sc. degree in physics from the Technical University of Eindhoven, Eindhoven, The Netherlands, in 1988.

He is currently with the Royal Netherlands Meteorological Institute (KNMI), De Bilt, The Netherlands, and is working on scatterometer data interpretation, inversion, calibration, validation, and quality monitoring.